# Chapter 7
# Airborne Wind Energy for Martian Habitats


**Roland Schmehl, Mario Rodriguez, Lora Ouroumova, and Mac Gaunaa**

**Abstract** Renewable energy for Mars habitats is of key interest for future crewed missions. However, the low solar irradiation and low atmospheric pressure on Mars pose serious challenges to exploiting these resources reliably. In this chapter, we investigate the technical feasibility of a soft-kite-based airborne wind energy system and its potential to power a subsurface Mars habitat in combination with photovoltaics and short-term electrical storage. We propose a soft kite for its high surface-to-mass ratio, compact packing volume, adaptability to the available wind resource, and, thus, high capacity factor. First, the siting of the habitat is outlined, and the wind resources are quantified in terms of the wind speed probability distribution at the operational height of the system for different seasonal periods. Then, a performance model for the pumping cycle operation is developed to compute the power curve of the airborne wind energy system. Combining this with the wind statistics, a process for predicting the electricity yield at the habitat location is developed, which is then used to size all components of the hybrid power system to meet the continuous electrical power demand of 10 kW of the envisioned habitat.

## Abbreviations

| | |
|---|---|
| AEP | Annual energy production |
| AWE | Airborne wind energy |
| DBDM | Dichotomy Boundary Deuteronilus Mensae |
| ESA | European Space Agency |
| EZ | Exploration zone |

R. Schmehl (✉) · M. Rodriguez · L. Ouroumova
Delft University of Technology, Faculty of Aerospace Engineering, Kluyverweg 1, 2629 HS Delft, The Netherlands
e-mail: r.schmehl@tudelft.nl

M. Rodriguez · M. Gaunaa
DTU Wind Energy, Airfoil and Rotor Design Wind Turbine Design Division, Frederiksborgvej 299, 4000 Roskilde, Denmark



A. Cervone et al. (eds.), *Adaptive On- and Off-Earth Environments*, Springer Series in Adaptive Environments, https://doi.org/10.1007/978-3-031-50081-7_7

| | |
|---|---|
| GCM | General Circulation Model |
| KCU | Kite control unit |
| LMD | Laboratoire de Météorologie Dynamique |
| LS | Solar longitude |
| MCD | Mars Climate Database |
| MOLA | Mars orbiter laser altimeter |
| NASA | National Aeronautics and Space Administration |
| OSIP | Open Space Innovation Platform |
| PCA | Principal component analysis |
| PDF | Probability density function |
| PM | Protonilus Mensae |
| PV | Photovoltaics |
| ROI | Region of interest |
| WRF | Weather research and forecasting model |

## 7.1 Introduction

Robotic missions to Mars are impressive attestations of the technological advancement in planetary exploration. While first landers established only stationary surface probes, and subsequent rover missions gradually increased the ground mobility, the recent Mars helicopter Ingenuity initiated an entirely new era of aerial mobility on Mars (NASA 2023). Governmental space agencies and private corporations have also proposed human missions to Mars with the goal of establishing habitats. However, compared to robotic missions, such endeavors will be extremely costly. Because of the limited transportation capacity, in situ material and energy utilization will be of crucial importance (Horneck et al. 2006).

Haslach (1989) explored the use of wind energy on Mars and found that despite the low atmospheric density, wind speeds would be sufficient to compete with nuclear power in terms of power produced relative to the transported mass. As part of the study, the design of a mobile and lightweight vertical-axis wind turbine was proposed while the variability of the wind was identified as a critical point requiring further attention. James et al. (2022) studied using local material and energy sources for a Martian outpost, covering geothermal, solar, and wind resources, and concluded that wind power would be a feasible energy source. Bluck (2001) considered the combined use of solar and wind energy systems for a sustainable Mars base. To compensate for the missing solar power during month-long Martian global dust storms, it was suggested to use modified cold-weather wind turbines. The more critical study of Delgado-Bonal et al. (2016) suggested that wind power on Mars would be ineffective because of the too-low wind speeds. Holstein-Rathlou et al. (2022) tested a lightweight horizontal axis wind turbine in the Aarhus Mars Simulation Wind Tunnel and concluded that wind power generation would be possible on Mars. The Danish start-up KiteX develops and markets a very similar, rapidly deployable,

and lightweight horizontal axis turbine with a rotor diameter of 2 m, a hub height of 4 m, and a rated power of 250 W at the rated wind speed of 5.5 m/s (KiteX 2023).

Schorbach and Weiland (2022) investigated the wind power potential at the Viking Lander 2 site during the 1977b global dust storm and concluded that towered turbines would be unsuitable as a backup energy source for Mars missions powered by solar photovoltaics (PV). Contrasting this, Hartwick et al. (2022) used a global climate model to investigate the total planetary Martian wind potential and determine its spatial and temporal variability. They found that the wind speeds at several future landing sites would be sufficiently high for a stand-alone or complementary energy source. They argued that the Viking lander sites were prioritized for low wind speeds so as not to complicate landing operations or contribute to instrument noise. Anhalzer et al. (2023) investigated the feasibility of using high-efficiency wind turbines with co-flow jet blades for recharging electric aircraft wind energy on Mars.

A more radical reduction of the structural mass can be achieved with airborne wind energy (AWE) systems (Hagen et al. 2023). The innovative technology is based on tethered flying devices and was also mentioned by Schorbach and Weiland (2022); Hartwick et al. (2022) as an interesting option for use on Mars. The use of kites for wind energy harvesting on Mars was first proposed by NASA researchers (Silberg 2012). Most of the currently pursued concepts convert the pulling power of the flying devices with a drum-generator module on the ground (Schmehl 2019). Another advantage next to the reduced mass is that the flight operation of the systems can be adjusted continuously to the available wind resource, by which the capacity factor can be maximized for a given wind profile (Bechtle et al. 2019). Major advances in automatic flight control over the past two decades have led to the commercial development of airborne wind energy for terrestrial applications (Vermillion et al. 2021; Fagiano et al. 2022). Several different implementations have reached the prototype stage (Nelson 2020).

In this chapter, we present a combination of airborne wind energy and solar PV systems with short-term battery storage to power the construction and subsequent use of a future subsurface Mars habitat. The primary AWE system is based on a remote-controlled flexible membrane kite operated in pumping cycles, alternating between reel-out and reel-in phases. Such a hybrid power plant was investigated by Reuchlin et al. (2023) for remote off-grid applications on Earth with the objective of minimizing the use of diesel fuel.

The baseline reference for the present study is the kite power system originally developed at TU Delft and tested extensively between 2010 and 2015. This development platform was based on a kite with a flattened wing surface area of 25 $m^2$, a suspended, remote-controlled cable robot denoted as a kite control unit (KCU), and a generator with a nominal electrical power of 18 kW, producing an average continuous power of about 7 kW at the rated ground wind speed of 7 m/s (Van der Vlugt et al. 2013, 2019). This power is sufficient for roughly 14 households in the Netherlands. Figure 7.1 shows the commercial scale-up of this system, further developed since 2016 by the university spin-off Kitepower B.V.

To adapt the system to the very different atmospheric conditions on Mars, the key design parameters of this kite power system are scaled to Martian conditions

**Fig. 7.1** Airborne wind energy system with 60 $m^2$ kite and suspended robotic control unit, operating on the Caribbean island Aruba in October 2021. Video still of the original drone footage with enhanced red tones (Schmehl 2022). Courtesy of Kitepower B.V.

using a novel method based on dimensional analysis. One of the main differences is that the much lower atmospheric density on Mars requires an increased surface area of the kite despite the higher wind velocities. The sizing and design of the kite power system are validated using a performance model expanding on earlier work of Luchsinger (2013); Fechner and Schmehl (2013). The complete microgrid solution also includes photovoltaic (PV) modules and electrical storage to buffer short-term (daily) periods of low wind.

The chapter summarizes and extends the work of two design synthesis exercises[1] at the Faculty of Aerospace Engineering of TU Delft (Corte Vargas et al. 2022; Gül et al. 2022), which contributed to a novel ideas competition on ESA's Open Space Innovation Platform (OSIP) and a subsequent interfaculty project with the European Space Agency (Bier et al. 2022; Bier 2022). The chapter also includes and extends the results of a follow-up MSc graduation project on the topic (Rodriguez 2022). The objective of this work is a performance analysis of the combined airborne wind energy and photovoltaic renewable energy solution, accounting for the demand and resource profiles and the coupling of all subsystems. Because only little quantitative information about the energy consumption of the robotic construction of the habitat was available at the time of the study, the design of the microgrid covers mainly the use of the habitat. It is planned also to integrate the construction phase in a future study.

[1] Graduation project of 10–11 Bachelor students who worked full-time for 10 weeks on an innovative system design in the field of aerospace engineering.

The chapter is structured as follows. In Sect. 7.2, the siting of the habitat is outlined and the wind resource is assessed at this location, using the Mars Climate Database. In Sect. 7.3, a performance model for the AWE system is developed, and the procedure of calculating the annual energy production of the AWE system at the habitat location is described. In Sect. 7.4, the model for the entire microgrid is developed and used to match the production and storage of electricity with the demand of the habitat by sizing the different microgrid components. In Sect. 7.5, the conclusions are presented.

## 7.2 Wind Resource Assessment

The first step for designing a wind energy system that can meet the power requirements of a Martian habitat is an assessment of the available wind resources. Our tool of choice is the Mars Climate Database (MCD), which provides meteorological data and predictions for any location on Mars along the year (Millour et al. 2018). In Sect. 7.2.1, we first describe the siting process for the envisioned habitat over the different phases of the research project. In Sect. 7.2.2, the MCD and its use for the wind resource assessment are outlined. In Sect. 7.2.3, the seasonal variation of hourly wind speed profiles at the habitat location is discussed for 12 representative days. In the final Sect. 7.2.4, the probability distributions of wind speeds per season are determined.

### *7.2.1 Habitat Site Selection*

The location of the habitat, and by that also the location of the hybrid power plant, was updated along several phases of the project timeline. The different proposed habitat locations are listed in Table 7.1, with the most up-to-date location, Arsia North, at the bottom.

The first proposed location was the Dichotomy Boundary Deuteronilus Mensae (DBDM) Exploration Zone (EZ), a circular area of 100 km (Head et al. 2015). It was chosen because NASA concluded that the location has potentially been habitable in the past, has potential for present habitability, and might have water ice closer

**Table 7.1** Chronology of proposed habitat locations

| Name | Coordinates | | Elevation (m) [a] | References |
|---|---|---|---|---|
| DBDM EZ | 39.11°N | 23.199°E | −3750 | Corte Vargas et al. (2022); Ouroumova et al. (2021) |
| PM ROI 1 | 42.109°N | 50.141°E | 0 | Gül et al. (2022) |
| Arsia South A | −14.377°N | 240.051°E | 8600 | Rodriguez (2022) |
| Arsia North | −3.062°N | 236.07°E | 4600 | Rodriguez (2022) |

[a] MOLA elevation

than 3 m below the surface. In the second project phase, the habitat was relocated to Protonilus Mensae (PM) Region of Interest (ROI) 1 (Gallegos et al. 2019) to exploit substantially better wind conditions that were identified by using the Mars Climate Database. In the third project phase, the habitat was relocated to Arsia South A to make use of existing lava tubes for the construction of the subsurface habitat. The characteristics of lava tubes on different planets are discussed in detail in Sauro et al. (2020), while the scouting using ground-penetrating radar and potential use for future space habitats are described in Qiu and Ding (2023). Because of the extremely high altitude of Arsia South A and the associated low atmospheric density, the habitat was eventually relocated to Arsia North, which is at a lower altitude, while featuring lava tubes with the required opening diameter for the habitat. The two locations on Arsia Mons are shown in Fig. 7.2. The average atmospheric properties at these two locations are compared to those at the Viking 1 lander site in Table 7.2. The wind resource analysis presented in the following sections is conducted for the final habitat site at Arsia North.

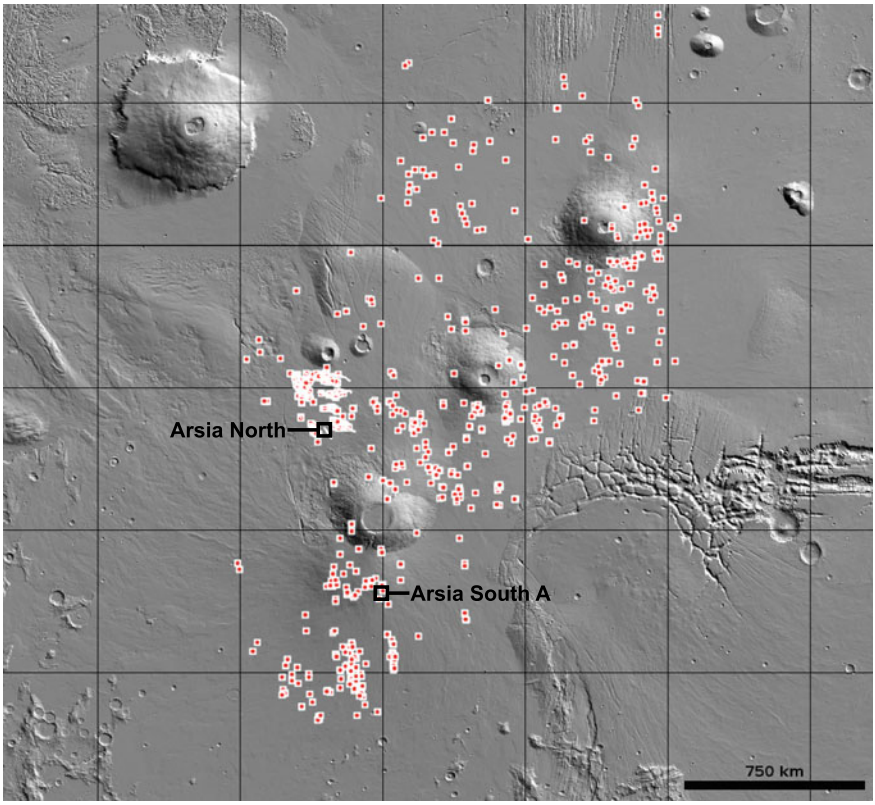


**Fig. 7.2** Location of candidate lava caves on the Tharsis bulge, adapted from Sauro et al. (2020). The cave on Arsia North, highlighted by the green circle, was eventually selected as a compromise between lower altitude, i.e., higher density, and reasonable wind speeds

**Table 7.2** Comparison of average atmospheric properties at habitat candidate locations Arsia South A and Arsia North and the Viking 1 lander site

| Physical property | Arsia North[a] | Arsia South A[a] | Viking 1 site[b] |
|---|---|---|---|
| Average wind speed (m/s) | 20 | 17 | 10 |
| Average density (kg/m$^3$) | 0.01 | 0.007 | 0.02 |

[a] Computed with MCD (Rodriguez 2022)
[b] Average wind speed from Boumis (2017), average density from Williams (2020)

### *7.2.2 Mars Climate Database*

The high temporal and spatial variability of the Mars climate results from the diurnal and seasonal cycles combined with an extreme and diversified topography and dust loading of the atmosphere (Laboratoire de Météorologie Dynamique 2023). The MCD models these variations of the Martian atmosphere and can be used to predict the wind resources at specific locations. The database provides meteorological fields derived from numerical simulations of the Martian atmosphere based on a General Circulation Model (GCM) and validated using measurement data (Forget et al. 1999; Millour et al. 2018). The GCM uses a grid with a step size of 5.625° in longitude and 3.75° in latitude, corresponding to a spatial resolution of 332.7 by 221.8 km, and 49 atmosphere levels (MCD v5.3). The raw lower-resolution GCM results can be combined with high-resolution (32 pixel/degree) Mars Orbiter Laser Altimeter (MOLA) topography records and smoothed Viking Lander 1 pressure records to yield high-resolution values of atmospheric variables. The much higher resolution of the MOLA data increases the spatial resolution to 1.85 km at the equator, where the grid is the largest.

The MCD allows the modeling of various conditions, such as the solar maximum, average, and minimum. These conditions can be combined with average climatological conditions and planetary-wide dust storm conditions. The model further allows the simulation of dusty conditions with solar maximum and low dust conditions. It is optionally possible to simulate specific conditions of certain years. The solar conditions of a day can be pre-determined since the solar activity is periodic, following an 11-year magnetic cycle that influences the solar irradiance. Since the wind cycle on Mars is primarily driven by irradiance, this periodicity can be used to predict wind conditions and, thus, the annual energy production (AEP) of the AWE system. During the design phase, it is crucial to consider both the maximum and the minimum conditions to produce a sufficient average power.

A limitation of the MCD is the non-linear vertical spacing of the GCM grid. The lowest level is 5 m above the surface, the highest at around 250 km, and the distance between levels increases with height. Consequently, the operational height range of the AWE system, which we consider in this study to be 0–400 m, is discretized by only five levels. Atmospheric data between the grid levels are evaluated by linear interpolation using the above-mentioned high-resolution post-processing mode, which means that extreme values generated by the GCM are not reflected in the

database. For this reason, Millour et al. (2018) expressed caution in using the MCD to estimate extreme values, such as diurnal ranges or spatial maxima and minima, with the database appearing to underestimate rapid rates of change in variables with space or time.

### *7.2.3 Seasonal Variation of Hourly Wind Speed Profiles*

The wind resource data available from the MCD is in hourly resolution. For time-keeping on Mars, we use either solar longitude, abbreviated as Ls and measured in degrees, or solar days, denoted as sols. The solar longitude describes the angle between Mars and the Sun measured from the Northern Hemisphere spring equinox where Ls = 0. A Martian sol is roughly equal to 24 h and 37 min on Earth and a Martian hour is 1/24 of a Martian sol. Because Mars moves slightly slower than Earth and is farther away from the Sun, a complete orbit, which is one Martian year, takes 687 d on Earth. The longer year means also that the seasons on Mars are longer. All times in this chapter are Martian times.

#### Hourly Vertical Wind Profiles

To get a first impression of the annual wind resource at the selected habitat location, Fig. 7.3 illustrates the development of the vertical wind speed profiles along 12 d representing different seasonal periods of the Martian year. Each contour plot is drawn with a resolution of 5 m in height and one hour in time, resulting in a total of 1440 data points per plot. The days are selected in steps of 30° solar longitude. The plots in the left column (Ls 0°, 90°, 180°, and 270°) represent the equinox constellations. The contour plots indicate when and where the highest wind speeds are experienced during the day. Comparing the seasons further indicates whether these periods of high wind speeds shift in time as the seasons change.

This annual wind resource overview reveals two daily recurring prominent periods of very low wind speeds over the entire investigated height range. The first period occurs roughly between 9:00 and 12:00, the second period roughly between 18:00 and 22:00, during which the wind speeds drop to almost zero over the entire height range. The kite will not be able to fly during these low-wind periods. On the other hand, high wind speeds consistently occur in the mornings, between 0:00 and 8:00, and in the afternoon, between 12:00 and 18:00. The highest wind speeds most often occur in the afternoons, with the maximum in late autumn when the wind speeds during the night are highest.

While wind speeds on Mars are generally much lower during the summer, this is not the case at the selected habitat location, Arsia North. This is thought to be caused by a low-altitude (500 m) cross-equatorial jet that can form during the northern hemisphere summer along the eastern flank of the Tharsis bulge (Joshi et al. 1995).

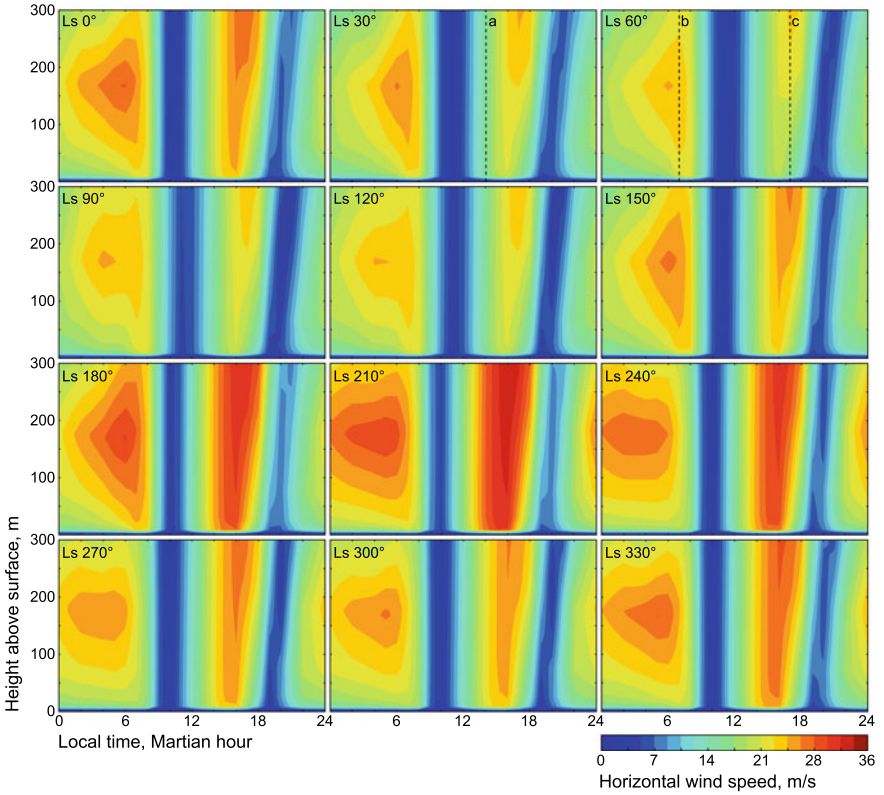


**Fig. 7.3** Development of the vertical wind speed profiles over 12 Martian days representative of the seasonal periods at Arsia North. Top left to bottom right: spring equinox, late spring, early summer, summer equinox, late summer, early autumn, autumn equinox, late autumn, early winter, winter equinox, late winter, and early spring. The labeled dashed lines in the late spring and early summer plots indicate the positions of the vertical wind profiles illustrated in Fig. 7.4 (Rodriguez 2022)

Figure 7.4 shows three characteristic vertical profiles extracted from the annual wind speed data. The profile on the left depicts a nearly uniform wind speed profile. The center profile depicts a typical low-level jet, where the wind speed first increases with height but then decreases again, while the profile on the right depicts the typical behavior of a shear flow along a surface, where the wind speed monotonically increases with height, often approximated by a logarithmic law. All profiles can be observed also on Earth (Schelbergen et al. 2020).

### Seasonal Average Hourly Wind Data

A second impression of the annual wind resource is given by Fig. 7.5 depicting the seasonal variation of the hourly wind speeds along the Martian day at five different heights. The wind speeds are averaged over the different seasonal periods, each

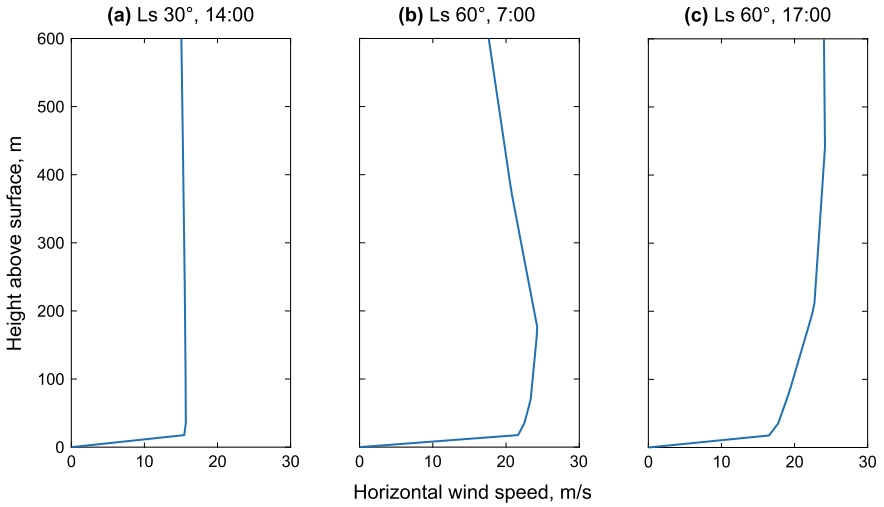


**Fig. 7.4** Characteristic vertical wind speed profiles extracted from the data shown in Fig. 7.3: **a** Uniform flow, **b** Low-level jet, and **c** Shear flow (Rodriguez 2022)

covering a solar latitude range of 45°. The analysis provides insight into the diurnal changes in the wind speed. The diagrams indicate that the highest wind speeds occur during the day and are strongest during autumn and winter. Assuming a cut-in wind speed of 9 m/s, a kite could fly at night at this specific location on Mars. This indication is consistent with the diurnal variations found in literature (Joshi et al. 1997). As already observed when discussing Fig. 7.3, flight operation will have to be discontinued for two short periods, roughly between 9:00 and 11:00 and between 19:00 and 21:00, during which the wind speed drops to relatively low values.

Also included are the all-season averages of the hourly wind speeds, summarized again for all five heights in the bottom-right diagram. Added here is the all-season average hourly wind speed at 127 m, which is the mid-altitude of the AWE system's reel-out phase. The wind speed data at this altitude will be used in Sect. 7.3 as input for the performance analysis.

### *7.2.4 Seasonal Variation of Wind Speed Probability Distribution*

The probability distribution of the wind speed at a specific location over a certain time period can be described in terms of a probability density function (PDF). This statistical measure is relevant not only for a better understanding of the local wind resources but is also a crucial input for the performance analysis of the AWE system described in Sect. 7.3. We use a Weibull distribution function to approximate the seasonal and annual probability distribution of the wind speeds at the habitat locations

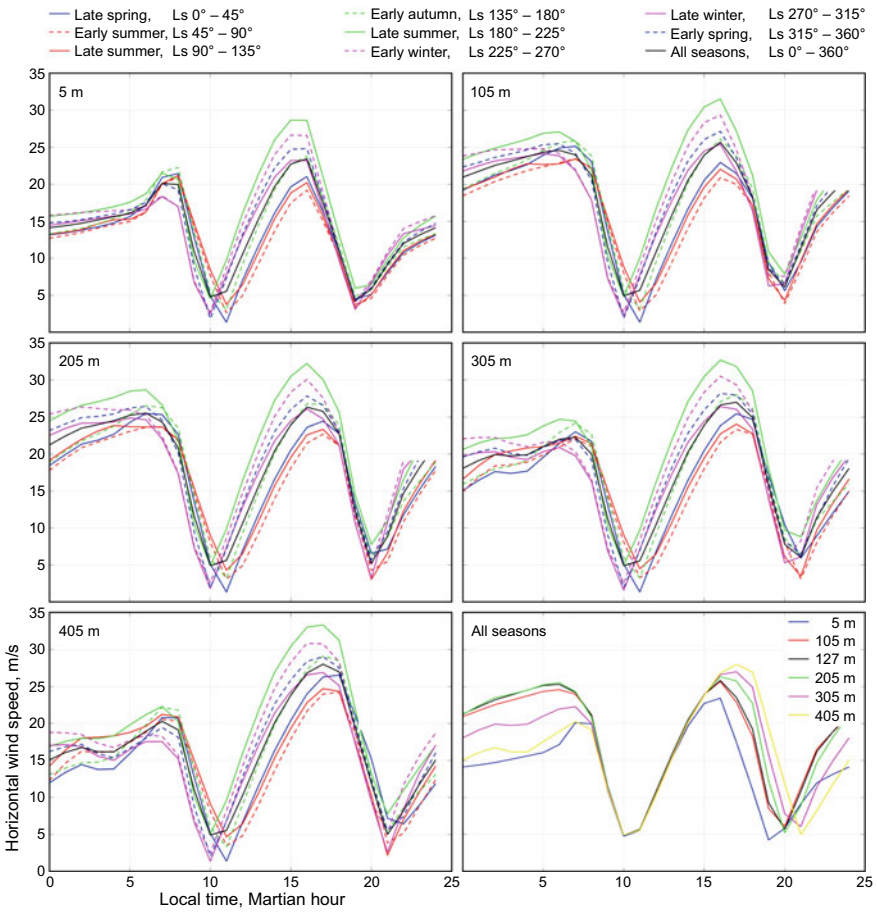


**Fig. 7.5** Average diurnal wind speed variation by season and by year at different heights (Rodriguez 2022)

$$g_{\mathrm{w}}\left(v_{\mathrm{w}}\right)=\frac{k}{v_{\mathrm{m}}}\left(\frac{v_{\mathrm{w}}}{v_{\mathrm{m}}}\right)^{k-1} e^{-\left(\frac{v_{\mathrm{w}}}{v_{\mathrm{m}}}\right)^{k}}, \tag{7.1}$$

where $v_{\mathrm{m}}$ is the scaling parameter and $k$ is the shape parameter.

Figure 7.6 shows the fitted distribution functions for the investigated eight seasonal periods at five different heights. Also included are the all-seasons averages of the distribution functions, summarized again for all five heights in the bottom-right diagram. The comparison shows that the highest average wind speeds do not occur at the maximum considered altitude, 405 m, but instead somewhere at mid-altitudes, between 105 and 205 m. This observation is consistent with the frequent occurrence of low-level jet wind profiles, such as depicted in Fig. 7.4(b), and it explains the choice of the height 127 m as the vertical center $z_{\mathrm{m,o}}$ of the cyclic power harvesting

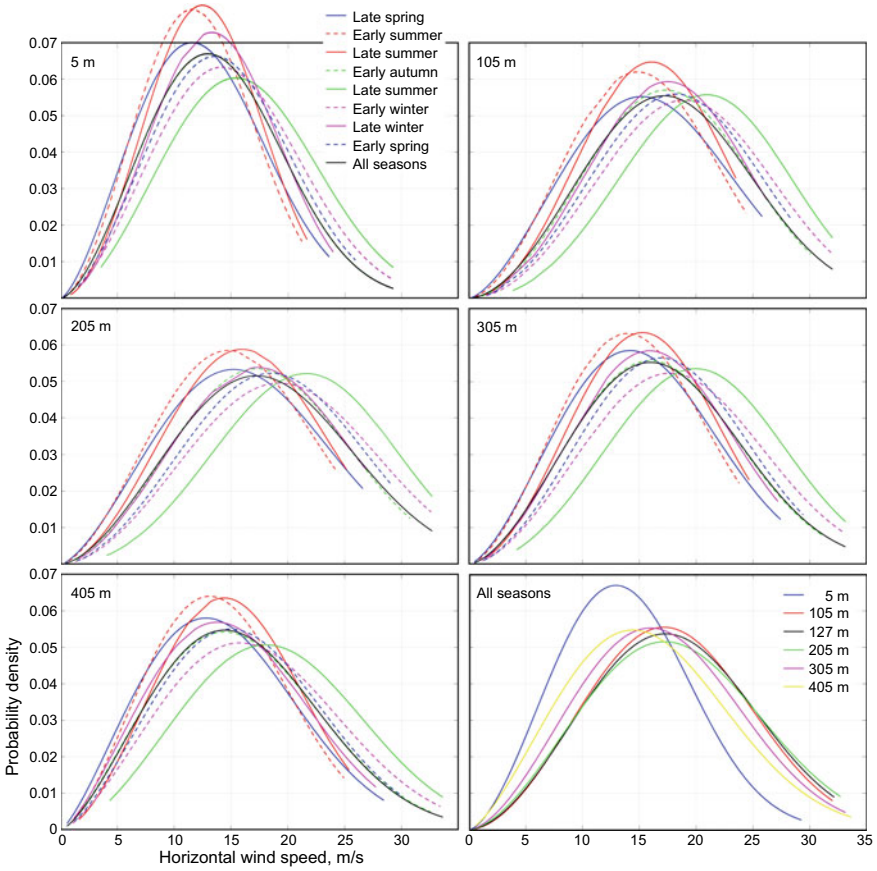


**Fig. 7.6** Probability density of hourly wind speeds for different seasonal periods and all-seasons average at different heights (Rodriguez 2022)

**Table 7.3** Weibull parameters of the wind speed data at the habitat location and the operational height for a subdivision of the Martian year into eight averaging periods specified in terms of solar longitude Ls (Rodriguez 2022)

| Ls range | 0–45 | 45–90 | 90–135 | 135–180 | 180–225 | 225–270 | 270–315 | 315–360 |
|---|---|---|---|---|---|---|---|---|
| $k$ | 2.495 | 2.668 | 2.941 | 2.847 | 3.314 | 2.952 | 2.950 | 2.913 |
| $v_m$, m/s | 18.754 | 17.726 | 18.573 | 20.280 | 23.691 | 22.067 | 20.270 | 21.261 |

operation, as discussed in the following Sect. 7.3. The parameters $v_m$ and $k$ of the Weibull distribution functions fitted to the wind speed data at this operating height, separated into eight seasonal periods, are listed in Table 7.3.

**Table 7.4** Weibull parameters of the wind speed data at the habitat location and the operational height for a subdivision of the Martian year into 16 averaging periods specified in terms of Martian days (Rodriguez 2022)

| Sols range | 0–43 | 44–88 | 89–133 | 134–179 | 180–224 | 225–269 | 270–312 | 313–352 |
|---|---|---|---|---|---|---|---|---|
| $k$ | 2.64 | 2.377 | 2.589 | 2.76 | 3.014 | 2.867 | 2.788 | 3.02 |
| $v_m$, m/s | 19.452 | 18.002 | 17.635 | 17.827 | 18.714 | 18.422 | 19.158 | 21.479 |
| Sols range | 353–391 | 392–430 | 431–468 | 469–507 | 508–545 | 546–585 | 586–626 | 627–668 |
| $k$ | 3.293 | 3.34 | 3.118 | 2.853 | 2.931 | 2.977 | 2.94 | 2.886 |
| $v_m$, m/s | 23.478 | 23.919 | 23.042 | 20.999 | 20.025 | 20.534 | 21.249 | 21.273 |

For the performance analysis of the AWE system, we use a finer subdivision of the Martian year into 16 seasonal periods of equal duration. The fitted parameters are listed in Table 7.4.

The proposed approach is suitable for the approximate yield estimation of the energy harvesting process. A more systematic approach for analyzing the statistics of the vertical wind speed profiles was presented in Schelbergen et al. (2020), using filtering and normalization of the wind speed data, followed by reducing their dimensions using a principal component analysis and $k$-means clustering into characteristic vertical profiles and their probabilities.

### 7.2.5 *Seasonal Variation of Atmospheric Density*

The seasonal variation of the atmospheric density at the habitat location and operational height is visualized in Fig. 7.7. The density varies up to 20% over the year

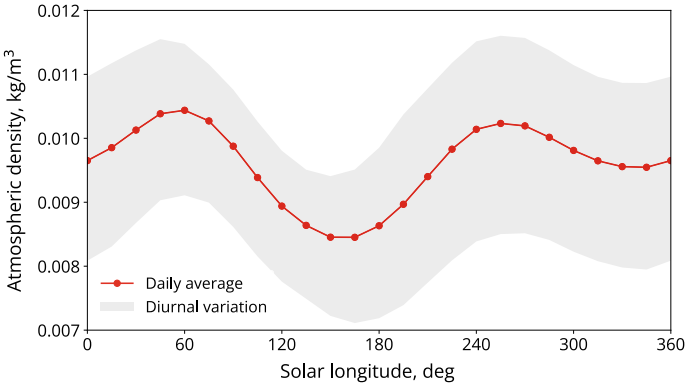


**Fig. 7.7** Variation of the atmospheric density at the habitat location and operational height over the Martian year

and also exhibits significant diurnal variations. The density decreases in summer and autumn, which is linked to the seasonal temperature increase causing the atmosphere to become thinner. Because these variations are substantial and because wind power linearly depends on density, we take the seasonal variation into account when computing the available wind power density at the habitat location and operational height of the AWE system.

## 7.3 Pumping Cycle Power

To accurately predict the achievable power output of the AWE system on Mars, the wind resource assessment has to be combined with an energy conversion model. As preparatory steps, the working principle and concept of operations of the considered pumping kite power system are outlined in Sect. 7.3.1, followed by a discussion of kite kinematics and key assumptions in Sect. 7.3.2. In Sect. 7.3.3, an analytical model is developed accounting for the reel-out and reel-in phases of the pumping cycle and the different aerodynamic loads, reeling speeds, and time durations. Following Terink (2009), each phase is described by a representative quasi-steady flight state. In Sect. 7.3.4, the conversion model is used for systematic optimization of the operational parameters, distinguishing three wind speed regimes with different operational strategies. The control concept was introduced by Luchsinger (2013); Fechner and Schmehl (2013) to account for constraints of a real implemented system. In Sect. 7.3.5, additional conversion losses are incorporated into the model, as proposed by Fechner and Schmehl (2013), to determine in Sect. 7.3.6 the net electrical power output of the system per production cycle, day, and year.

### *7.3.1 Working Principle and Concept of Operations*

The general working principle of an AWE system operated in pumping cycles is illustrated in Fig. 7.8. The diagram depicts a representative cycle trajectory in the wind reference frame, spanned by the $x_w$-, $y_w$-, and $z_w$-axes. The origin of this reference frame is located at the point where the tether exits from the ground station's drum, the $x_w$-axis is pointing in the direction of the wind, and the $z_w$-axis vertically upwards (Schmehl et al. 2013).

During the reel-out phase, the kite is operated in crosswind maneuvers, in the illustrated case, consecutive figure-of-eight patterns, maximizing the pulling force and thus also the generated energy. In the literature, this phase is also denoted as the traction or production phase. When reaching the maximum deployed tether length, the crosswind maneuvers are terminated, and the kite is depowered and steered into the $x_w z_w$-plane. To depower the kite, its rear bridle lines are released such that the wing pitches forward to a lower angle of attack with the relative flow. This substantially decreases the aerodynamic forces. In this outer transition phase, the

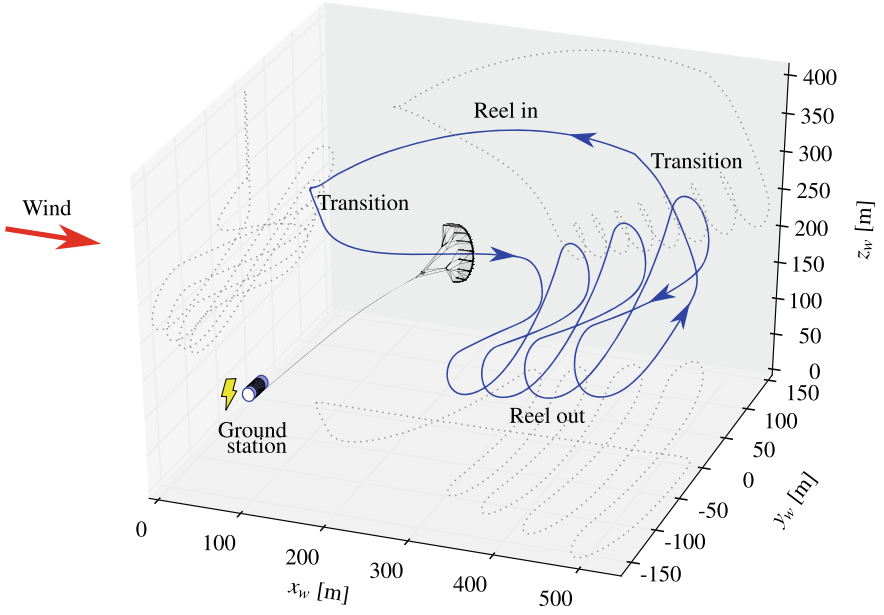


**Fig. 7.8** Flight path of a soft-kite-based pumping AWE system computed in the wind reference frame with a dynamic system model (adapted from Fechner 2016). Kite and drum not to scale

tether is kept at a constant length while the kite flies toward the $z_w$-axis continuously increasing its elevation angle. Before reaching the $x_w z_w$-plane and a static flight state, the ground station generally starts to reel in the tether.

During the reel-in phase, energy is consumed because the drum works against the pulling force of the kite, which is much lower than in the reel-out phase but still required to keep the airborne system under tension. In the literature, this phase is also denoted as the retraction or consumption phase. For the same reasons of structural stability, a soft-kite-based system can only be depowered to a certain degree. Consequently, the aerodynamic lift-to-drag ratio is still relatively high, which leads to a continuous increase in the elevation angle when reeling in. This process is also used for winch launching a kite from the ground or step towing to keep the kite airborne despite a too-low wind speed. When reaching the minimum deployed tether length, the kite is powered again by pulling in the rear bridle lines. In this inner transition phase, the tether is kept at a constant length while the kite flies toward the $x_w$-axis, continuously decreasing its elevation angle. Before reaching a static flight state, the crosswind maneuvers are reinitiated, and the ground station starts to reel out the tether, starting the next pumping cycle.

The net generated energy per cycle is the difference between the energy generated in the reel-out phase and the energy consumed in the reel-in phase. This latter amount of energy has to be stored suitably during the reel-out phase. Most currently implemented smaller-scale systems use rechargeable batteries or supercapacitors,

while other options, such as hydraulic drivetrains with pneumatic storage, might be of interest for larger-scale implementations (Hagen et al. 2023). In practice, the transition phases are generally kept as short as possible to minimize the associated losses in net power. For a soft-wing kite system, the depowering and powering of the wing takes a few seconds and is blended into the reel-in and reel-out phases.

During the reel-in phase and the two transition phases, the flight control system aims to keep the flight motion of the kite within the $x_w z_w$-plane, such that the flight path is roughly two-dimensional. During the reel-out phase, the kite is steered along three-dimensional, outgoing figure-of-eight maneuvers. In contrast to a wind turbine, pumping crosswind AWE systems thus harvest from a larger volume of the atmosphere.

Launching and landing do not contribute to energy harvesting but are indispensable operational phases to start up and shut down the pumping cycle operation. For example, when a thunderstorm approaches or other hazardous conditions are foreseeable, the kite must be landed, secured, and stored safely before it can eventually be launched again. Similarly, when the wind speed drops below the cut-in wind speed for an extended time period, the kite has to be landed and relaunched once the wind picks up again. For shorter periods, the kite can be kept airborne using the energy-consuming technique of step towing.

More details about the concept of operations are provided in Van der Vlugt et al. (2013, 2019), Salma et al. (2019).

### *7.3.2 Kite Kinematics and Key Assumptions*

The control system of the AWE system governs two distinctly different motion components of the kite. The component along the tether is imposed by the reeling speed of the ground station. The component in the plane perpendicular to the tether can be described by a flight direction and speed. The direction is controlled by the steering mechanism of the kite control unit. On the other hand, the flight speed cannot be controlled directly because a kite does not have a propulsion system. Instead, it is influenced by several factors, among others, the aerodynamic characteristics of the kite, most importantly the lift-to-drag ratio, the reeling speed, and the degree of alignment of flight direction and gravitational acceleration. The strong aerodynamic coupling of the two orthogonal motion components and the dominant effect of the flight speed on the pulling force explains why reliable and robust control of a kite in a varying and fluctuating wind environment still constitutes a challenge for the commercial development of AWE systems.

The described control concept and kinematic decomposition are applicable during flight phases of constant tether sag. Since the tether shape is determined by the equilibrium of the distributed load along the tether, such as aerodynamic drag, gravity, centrifugal acceleration, and the tether forces at both ends, sudden changes in these contributions also affect the tether sag. A changing sag, in turn, leads to a rotation of

**Fig. 7.9** Kite performing crosswind flight maneuvers with practically straight tether while reeling out (left) and non-maneuvering kite with strongly sagging tether while reeling in (right). Photographic footage with traced tether from 2 August 2012

the kite with respect to the ground station. This can be observed, for example, when powering or depowering the kite or when starting or stopping crosswind maneuvers.

Figure 7.9 illustrates the different tether geometries during reel out and reel in. While the tether is practically straight when flying crosswind maneuvers during reel-out, this particular flight test shows a rather extreme tether sag during reel-in, mainly because of low wind and reel-in speeds leading to a relatively low tether force. It should be noted that the photos do not depict the regular pumping cycle operation of the kite but the launching and landing phases with a relatively short deployed tether length, using an experimental setup with a tilted mast (Van der Vlugt et al. 2019; Salma et al. 2019).

A simplified mathematical model of tethered flight and tractive power generation can be derived by assuming a straight and inelastic tether. Using spherical coordinates $(r, \phi, \beta)$, the position of the kite in the wind reference frame can be described by the radial distance $r$ of the kite from the ground station, which is identical to the deployed tether length $l_\mathrm{t}$, the azimuth angle $\phi$ measured from the $x_\mathrm{w}z_\mathrm{w}$-plane, and the elevation angle $\beta$ measured from the ground plane. The flight velocity $\mathbf{v}_\mathrm{k}$ of the kite can be described by radial and tangential components $\mathbf{v}_{\mathrm{k,r}}$ and $\mathbf{v}_{\mathrm{k},\phi}$, respectively. The radial speed $v_{\mathrm{k,r}}$ is identical to the reeling speed $v_\mathrm{t}$ of the tether. It is positive for reel-out and negative for reel-in. The tangential velocity component is defined by the speed $v_{\mathrm{k},\phi}$ and the course angle $\chi$, measured in the local tangential plane $\tau$ from a defined reference direction. By definition, the tangential speed $v_{\mathrm{k},\phi}$ cannot be negative (Schmehl et al. 2013).

Figure 7.10 illustrates the definition of the kite's position and velocity in spherical coordinates. The magnitudes of the radial and tangential components of the flight velocity can be nondimensionalized with the wind speed,

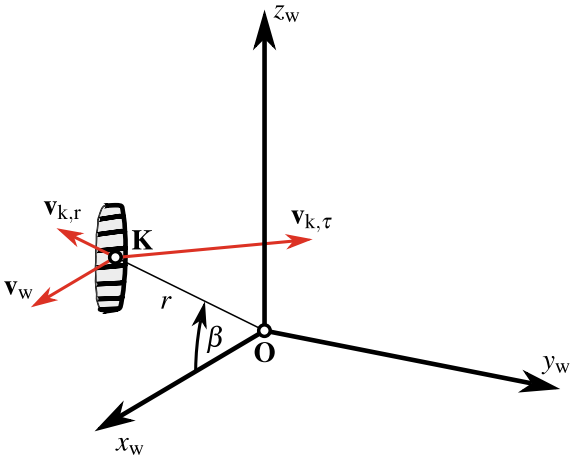


**Fig. 7.10** Kite with an idealized straight tether of variable length $r$ at elevation angle $\beta$ for the special case of the kite just passing through the $x_w z_w$-plane ($\phi = 0$)

$$\frac{v_k}{v_w} = \sqrt{f^2 + \lambda^2}, \tag{7.2}$$

$$f = \frac{v_{k,r}}{v_w} = \frac{v_t}{v_w}, \tag{7.3}$$

$$\lambda = \frac{v_{k,\phi}}{v_w}, \tag{7.4}$$

introducing the reeling factor $f$ and the tangential velocity factor $\lambda$.

Figure 7.11 shows a side view of the three-dimensional flight path depicted in Fig. 7.8. The pumping cycle evolves through six characteristic points in times, $t_0 - t_1 - t_2 - t_3 - t_4 - t_5$. Following a convention introduced by Van der Vlugt et al. (2019), the start time $t_0$ of the cycle is set to the end of the reel-out phase. In this schematic, the angle $\beta_o$ describes the average elevation angle during reel out with the nondimensional speed $f_o$, while the angle $\beta_i$ describes the constant elevation angle during steady-state reel-in with the constant nondimensional speed $f_i$. It should be noted that this asymptotic limit state is not necessarily reached, as it is depicted in Fig. 7.11. Depending on the aerodynamic properties of the depowered kite, its mass, the reel-in speed, and the covered radial distance $r_{max} - r_{min}$, the reel-in phase may end at $t_3$ before reaching the steady-state flight condition with constant elevation angle $\beta_i$. The parameter $z_{m,o}$ describes the mid-altitude of the reel-out phase, which will be used to evaluate the wind resource accessible for conversion.

Table 7.5 describes how the position and the nondimensional velocity variables vary along the phases of the pumping cycle. The first part of the reel-in phase is described by $\lambda > 0$ and increasing elevation angle $\beta$, while the second part of the steady-state reel-in is described by $\lambda = 0$ and constant elevation angle $\beta_i$.

To assess the generated and consumed energies over a pumping cycle, we need to identify one or more representative flight states for each phase and, from these, estimate the respective pulling force of the kite. The most basic approach uses one

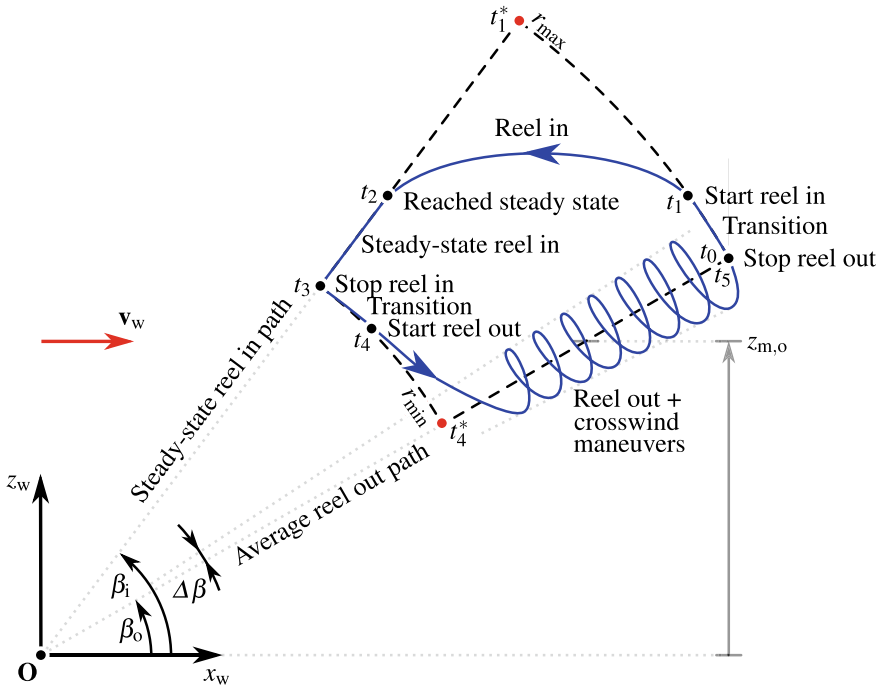


**Fig. 7.11** Side view of real (solid blue) and idealized (dashed) flight paths

**Table 7.5** Phases of pumping cycle operation of a soft-wing kite

| Start time | Name | Kite position | | | Kite velocity | | |
|---|---|---|---|---|---|---|---|
| | | $r$ | $\phi$ | $\beta$ | $f$ | $\lambda$ | $\chi^a$ |
| $t_0$ | Outer transition | $r_{max}$ | $\to 0$ | $\nearrow$ | 0 | $> 0$ | $\to 0$ |
| $t_1$ | Reel-in | $\searrow$ | $\approx 0$ | $\nearrow$ | $f_i < 0$ | $> 0$ | $\approx 0$ |
| $t_2$ | Steady-state reel-in | $\searrow$ | $\approx 0$ | $\beta_i$ | $f_i < 0$ | 0 | $\approx 0$ |
| $t_3$ | Inner transition | $r_{min}$ | $\approx 0$ | $\searrow$ | 0 | $> 0$ | $\to \pi$ |
| $t_4$ | Reel-out | $\nearrow$ | $\pm\Delta\phi$ | $\beta_o \pm \Delta\beta$ | $f_o > 0$ | $\gg 0$ | $\pm\pi$ |
| $t_5$ | Outer transition | … | | | | | |

[a] Course angle relative to the local upwards direction $\mathbf{e}_\beta$, as in Fechner and Schmehl (2018)

flight state for the reel-out phase and a separate one for the reel-in phase (Terink 2009; Luchsinger 2013). A suitable choice for the reel-out phase is a crosswind flight condition at the average elevation angle $\beta_o$, while for the reel-in phase, it is the steady flight state at the asymptotic limit angle $\beta_i$. The corresponding idealized flight path is included as a dashed line $t_0 - t_1^* - t_3 - t_4^* - t_5$ in Fig. 7.11. The approximation entails that the transition phases are infinitely fast, i.e., $t_1^* = t_0$ and $t_4^* = t_3$, such that the pumping cycle operation practically switches between reel-out and reel-in flight states. Because the transition phases are periods of zero power generation, they represent losses of net power. To maximize the cycle power, the transition phases will be shortened to a minimum feasible duration, which means that the approximation should be quite reasonable for any optimized commercial AWE system. In the next section, the two representative flight states will be used to estimate the net power over a pumping cycle.

Formulating the mathematical model in terms of nondimensional parameters $f$ and $\lambda$ defined by Eqs. (7.3) and (7.4) is important for investigating how airborne wind energy generation scales from the conditions on Earth to those on Mars. However, in a realistic wind field, the wind speed varies in space and time. The question arises of which wind speed value is most suitable to characterize the energy conversion process. Given that the kite harvests wind energy over a large altitude range, the variation of the wind speed with altitude is important to consider. Because the power output of the reel-out phase is ruling for the net energy produced, the mid-altitude of this phase will be used, as suggested by Van der Vlugt et al. (2019) and indicated in Fig. 7.11

$$z_{m,o} = \frac{1}{2}\left(r_{min} + r_{max}\right)\sin\beta_o. \tag{7.5}$$

The tractive power of the kite is the product of the tether force and the reeling speed at the ground station. The dominant contribution to the tether force is the resultant aerodynamic force of the kite, commonly represented as a combination of lift and drag components

$$\mathbf{F}_a = \mathbf{L} + \mathbf{D}, \qquad \text{with} \tag{7.6}$$

$$L = \frac{1}{2}\rho v_a^2 C_L S, \tag{7.7}$$

$$D = \frac{1}{2}\rho v_a^2 \left(C_{D,k} S + \frac{1}{4} C_{D,t} d_t r\right), \tag{7.8}$$

where $\rho$ is the atmospheric density, $C_L$ and $C_{D,k}$ are the lift and drag coefficients, and $S$ the planform area of the kite, respectively, $C_{D,t}$ is the drag coefficient of a cylinder in a cross flow, and $d_t$ is the tether diameter (Van der Vlugt et al. 2019). Equation (7.8) can be reformulated in terms of a lumped drag coefficient $C_D$

$$D = \frac{1}{2}\rho v_a^2 C_D S, \qquad \text{with} \tag{7.9}$$

$$C_D = C_{D,k} + \frac{1}{4} C_{D,t} \frac{d_t r}{S}. \tag{7.10}$$

Similarly to the argument presented for Eq. (7.5, we use in this approximation the mean tether length during the reel-out phase

$$r_{m,o} = \frac{1}{2}\left(r_{min} + r_{max}\right). \tag{7.11}$$

By definition, the drag component **D** is aligned with the apparent wind velocity $\mathbf{v}_a$ while the lift component **L** is perpendicular to it. The apparent wind velocity is defined as the relative flow velocity at the kite

$$\mathbf{v}_a = \mathbf{v}_w - \mathbf{v}_k. \tag{7.12}$$

Inserting Eqs. (7.7) and (7.9) into Eq. (7.6) and making use of the orthogonality of the two force components, the magnitude of the aerodynamic force can be evaluated as

$$F_a = \frac{1}{2}\rho C_L \sqrt{1 + \frac{1}{E^2}} S v_a^2, \tag{7.13}$$

where $E$ denotes the lift-to-drag ratio $L/D$ of the kite.

Because of the low mass and large wing surface area of membrane kites, inertial forces play only a minor role, and the kite's motion can be assumed to be quasi-steady. Furthermore, in the power production phase, the aerodynamic force is substantially larger than the gravitational force acting on the kite, and as a consequence, the tether force can be approximated by the tether force

$$0 = \mathbf{F}_t + \mathbf{F}_a. \tag{7.14}$$

Accordingly, the nondimensional tether force and tractive power can be derived as

$$\frac{F_t}{qS} = C_L \sqrt{1 + \frac{1}{E^2}} \left(\frac{v_a}{v_w}\right)^2, \tag{7.15}$$

$$\zeta = \frac{P}{P_w S} = C_L \sqrt{1 + \frac{1}{E^2}} f \left(\frac{v_a}{v_w}\right)^2, \tag{7.16}$$

where $q$ denotes the dynamic wind pressure and $P_w$ the wind power density,

$$q = \frac{1}{2}\rho v_w^2, \tag{7.17}$$

$$P_w = \frac{1}{2}\rho v_w^3. \tag{7.18}$$

The nondimensional power $\zeta$ defined by Eq. (7.16) is also denoted as power harvesting factor (Diehl 2013; Schmehl et al. 2013; Vander Lind 2013).

### 7.3.3 Kite Mechanical Power Generation

The net mechanical energy of a pumping cycle is the difference between the generated and consumed energies during the reel-out and reel-in phases, respectively. Applying the idealizations outlined in the previous section, these energies can be estimated with Eq. (7.16), using the wind power density $P_\mathrm{w}$ at the location, the planform area $S$ and aerodynamic properties $C_\mathrm{L}$ and $E$ of the kite, the reeling factor $f$, and the nondimensional apparent wind speed $v_\mathrm{a}/v_\mathrm{w}$ in each cycle phase.

#### Apparent Wind Speed, Tether Force, and Mechanical Power

A general expression for $v_\mathrm{a}/v_\mathrm{w}$ can be derived by decomposing the velocity vector into radial and tangential components,

$$\mathbf{v}_\mathrm{a} = \mathbf{v}_\mathrm{a,r} + \mathbf{v}_\mathrm{a,\phi}, \tag{7.19}$$

and then, using the orthogonality of the components to formulate the velocity magnitude, as

$$\frac{v_\mathrm{a}}{v_\mathrm{w}} = \frac{v_\mathrm{a,r}}{v_\mathrm{w}}\sqrt{1+\left(\frac{v_\mathrm{a,\phi}}{v_\mathrm{a,r}}\right)^2}. \tag{7.20}$$

The radial velocity component in this expression can be derived from the radial component of Eq. (7.12),

$$v_\mathrm{a,r} = v_\mathrm{w,r} - v_\mathrm{k,r}, \tag{7.21}$$

substituting $v_\mathrm{w,r} = \cos\beta v_\mathrm{w}$, as illustrated in Fig. 7.10, and $v_\mathrm{k,r} = f v_\mathrm{w}$, according to Eq. (7.3), to get

$$\frac{v_\mathrm{a,r}}{v_\mathrm{w}} = \cos\beta - f. \tag{7.22}$$

This expression implies $\phi = 0$. For an arbitrary azimuth angle, an additional orthogonal projection into the $x_\mathrm{w}z_\mathrm{w}$-plane needs to be applied, multiplying $\cos\beta$ by $\cos\phi$ (Schmehl et al. 2013).

Assuming that the flight motion of the kite is governed by the quasi-steady equilibrium of the resultant aerodynamic force and the tether force only, it can be shown that the ratio $v_\mathrm{a,\phi}/v_\mathrm{a,r}$ is identical to the lift-to-drag ratio of the kite (Schmehl et al. 2013)

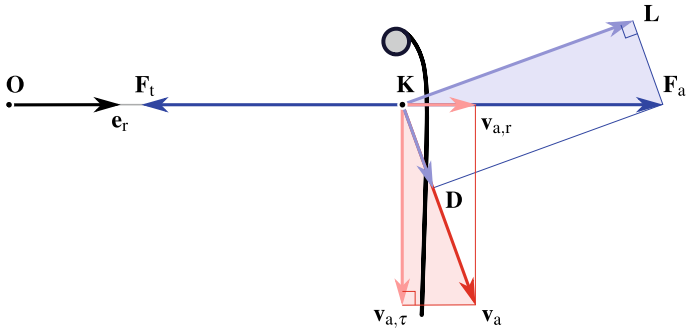


**Fig. 7.12** Quasi-steady force equilibrium governing the flight motion of a massless kite, with apparent wind velocity components $\mathbf{v}_{a,\tau}$ and $\mathbf{v}_{a,r}$, and aerodynamic force components $\mathbf{L}$ and $\mathbf{D}$, in the plane spanned by the apparent wind velocity $\mathbf{v}_\mathrm{a}$ and the resultant aerodynamic force $\mathbf{F}_\mathrm{a}$

$$\frac{v_{\mathrm{a},\emptyset}}{v_{\mathrm{a,r}}} = \frac{L}{D} = E. \tag{7.23}$$

This fundamental identity derives from the geometric similarity of the velocity and force triangles illustrated in Fig. 7.12. Because the vectors $\mathbf{v}_\mathrm{a}$ and $\mathbf{L}$ are perpendicular by definition, and the vectors $\mathbf{v}_{\mathrm{a},\emptyset}$ and $\mathbf{F}_\mathrm{a}$ are perpendicular by assumption of $\mathbf{F}_\mathrm{a} + \mathbf{F}_\mathrm{t} = 0$, and because the colored velocity and force triangles are right triangles, the two triangles are also geometrically similar.

Inserting Eqs. (7.22) and (7.23) into Eq. (7.20) leads to the following algebraic expression for the nondimensional apparent wind speed experienced by a kite flying in the $x_\mathrm{w}z_\mathrm{w}$-plane

$$\frac{v_\mathrm{a}}{v_\mathrm{w}} = \sqrt{1+E^2}\,(\cos\beta - f)\,, \tag{7.24}$$

describing the dependency on the operational parameters $\beta$ and $f$ and the design parameter $E$. The speed is unaffected by the flight direction, decreases with increasing elevation angle and reeling factor, and increases with $E$. Inserting Eq. (7.24) into Eqs. (7.15) and (7.16) leads to

$$\frac{F_\mathrm{t}}{qS} = C_\mathrm{L}\sqrt{1+\frac{1}{E^2}}\left(1+E^2\right)(\cos\beta - f)^2\,, \tag{7.25}$$

$$\frac{P}{P_\mathrm{w}S} = C_\mathrm{L}\sqrt{1+\frac{1}{E^2}}\left(1+E^2\right) f\,(\cos\beta - f)^2\,. \tag{7.26}$$

During the reel-out phase, the kite is generally flown with a high lift-to-drag ratio to maximize the tether force and the generated power. In this case, for $E \gg 1$, Eqs. (7.24, (7.25), and (7.26) further simplify to

$$\frac{v_\mathrm{a}}{v_\mathrm{w}} = E\,(\cos\beta - f)\,, \tag{7.27}$$

$$\frac{F_\mathrm{t}}{qS} = C_\mathrm{L}E^2\,(\cos\beta - f)^2\,, \tag{7.28}$$

$$\frac{P}{P_\mathrm{w}S} = C_\mathrm{L}E^2 f\,(\cos\beta - f)^2\,. \tag{7.29}$$

Equations (7.24), (7.25), (7.26), (7.27), (7.28), and (7.29) describe the relative flow velocity, tether force, and tractive power of a massless kite in the $x_\mathrm{w}z_\mathrm{w}$-plane over the whole pumping cycle.

The ground station controls the reeling factor $f$. During crosswind flight, the tangential velocity factor $\lambda$ adjusts to the instantaneous position and flight direction along the trajectory, depending on the kite's aerodynamic characteristics (Schmehl et al. 2013). During steady-state reel-in, the tangential motion component of the kite is zero. The aerodynamic characteristics of the kite are now a function of the reeling speed and the desired descent angle. This specific flight condition will be investigated in the following.

### Reel-In Phase

The situation during steady-state reel-in is depicted in Fig. 7.13. To descend with a constant elevation angle $\beta$, the kite velocity $\mathbf{v}_\mathrm{k}$ has to align with the tether. For this specific flight mode, Eq. (7.12) can be developed into an alternative algebraic expression for the nondimensional apparent wind speed

$$v_\mathrm{a}^2 = (v_\mathrm{w} + \cos\beta v_\mathrm{k})^2 + (\sin\beta v_\mathrm{k})^2\,, \tag{7.30}$$

$$= v_\mathrm{w}^2 + 2v_\mathrm{w}v_\mathrm{k}\cos\beta + v_\mathrm{k}^2, \tag{7.31}$$

$$\frac{v_\mathrm{a}}{v_\mathrm{w}} = \sqrt{1 - 2f\cos\beta + f^2}. \tag{7.32}$$

Equation (7.30) is constructed as a geometric relation assuming positive wind and kite speeds. The minus sign in Eq. (7.32) accounts for the negative value of $f$ during reel-in. The above derivation is based solely on the kinematic requirement of aligning the kite velocity vector with the tether. Forces are not considered in this derivation. As seen from Fig. 7.13, the requirement of aligning the resultant aerodynamic force vector with the tether to satisfy the quasi-steady force equilibrium introduces a coupling of the lift and drag components. Consequently, a desired combination of descent path angle $\beta$ and reeling factor $f$ will require a specific lift-to-drag ratio $E$ value. This relationship can be derived formally following Loyd's theory for the simple (non-crosswind) kite, adapted for the case of reeling in the tether.

As illustrated in Fig. 7.13, the kite velocity $\mathbf{v}_\mathrm{k}$ can be decomposed into components $\mathbf{c}$ and $\mathbf{b}$ aligned with and perpendicular to the apparent wind velocity. Using these to substitute $\mathbf{v}_\mathrm{a}$ in Eq. (7.12) gives

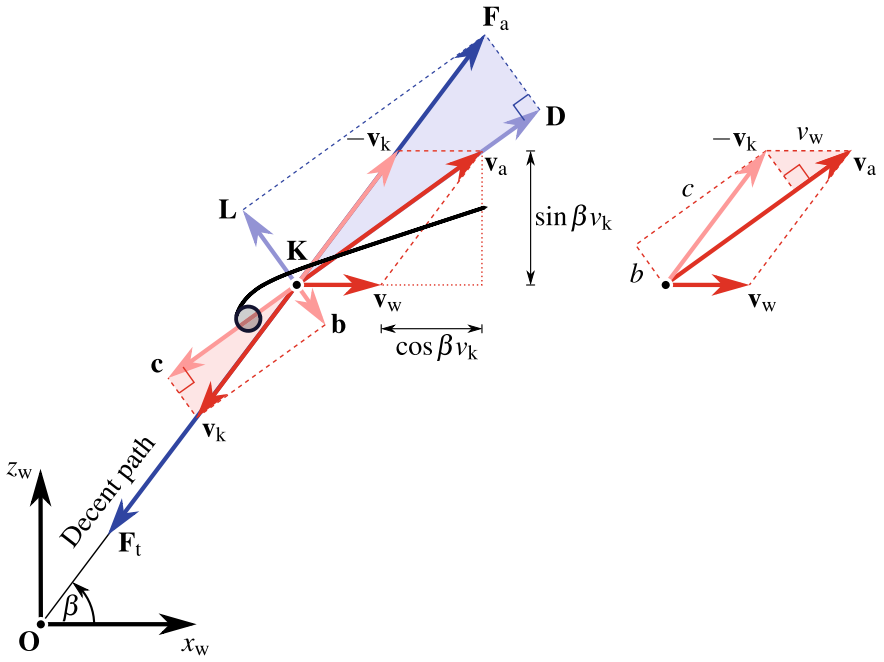


**Fig. 7.13** Steady-state reel-in of a massless kite at constant elevation angle $\beta$

$$\mathbf{v}_\mathrm{a} = \mathbf{v}_\mathrm{w} - \mathbf{b} - \mathbf{c}, \tag{7.33}$$

$$v_\mathrm{w}^2 = (v_\mathrm{a} - c)^2 + b^2, \tag{7.34}$$

where we again assume that $c$ and $b$ are positive speeds. Equation (7.34) is visualized in Fig. 7.13 by the colored triangle included in the right-hand side detail. Considering then the geometric similarity of the colored velocity and force triangles on the left-hand side of Fig. 7.13, we can derive the following relations:

$$\frac{b}{v_\mathrm{k}} = \frac{L}{F_\mathrm{a}} = \frac{1}{\sqrt{1 + \frac{1}{E^2}}}, \tag{7.35}$$

$$\frac{c}{v_\mathrm{k}} = \frac{D}{F_\mathrm{a}} = \frac{1}{\sqrt{1 + E^2}}, \tag{7.36}$$

which are further normalized to the wind speed to

$$\frac{b}{v_\mathrm{w}} = -\frac{f}{\sqrt{1 + \frac{1}{E^2}}}, \tag{7.37}$$

$$\frac{c}{v_\mathrm{w}} = -\frac{f}{\sqrt{1 + E^2}}. \tag{7.38}$$

As in Eq. (7.32), the minus signs in Eqs. (7.37) and (7.38) account for the negative value of $f$ when reeling in, to render positive values for the two speed ratios. Combining Eqs. (7.34, (7.37), and (7.38) and solving for the nondimensional apparent wind speed lead to the following expression:

$$\frac{v_\mathrm{a}}{v_\mathrm{w}} = \sqrt{1 - \frac{f^2}{1 + \frac{1}{E^2}}} - \frac{f}{\sqrt{1 + E^2}}, \tag{7.39}$$

$$= \frac{\sqrt{1 + E^2\left(1 - f^2\right)} - f}{\sqrt{1 + E^2}}. \tag{7.40}$$

While Eq. (7.32) describes the influence of the elevation angle and reeling speed on the apparent wind speed, Eq. (7.40) describes the influence of the lift-to-drag ratio and reeling speed. Although derived here for the reel-in phase with $f < 0$, both equations are equally valid for the reel-out phase with $f > 0$. Combining the two equations and solving for the lift-to-drag ratio give

$$E = \frac{\sqrt{1 - \cos^2\beta}}{\cos\beta - f} = \frac{\sin\beta}{\cos\beta - f}. \tag{7.41}$$

To maintain the steady-state descent of a massless kite with a given reel-in speed and elevation angle, a lift-to-drag ratio according to Eq. (7.41) has to be enforced. For $f = 0$, Eq. (7.41) reduces to the known result $E = \tan\beta$.

Combining Eqs. (7.24) and (7.40), we can further derive an expression for the elevation angle of a kite flying along a radial flight path, i.e., with $\lambda = 0$, toward or away from the ground attachment point,

$$\cos\beta = \frac{\sqrt{1 + E^2(1 - f^2)} + fE^2}{1 + E^2}. \tag{7.42}$$

This equation can be used to determine the maximum elevation angle $\beta_\mathrm{max}$ that a kite with a lift-to-drag ratio $E$ can assume during steady-state flight operation with a reeling factor $f$.

Equation (7.40) gives rise to an important operational constraint for the steady-state retraction of a massless kite. Requiring that the radicand in the numerator is larger or equal to zero leads to the following condition for the reeling factor

$$f \geq -\sqrt{1 + \frac{1}{E^2}}. \tag{7.43}$$

This limit shows that a very low lift-to-drag ratio is needed for fast reel-in. For $E \gg 1$ the minimum reeling factor is $-1$, while for $E = 1$ it only decreases to $-\sqrt{2}$. Since the tether force is relatively low during the reel-in phase, it can be assumed that

the gravitational forces neglected in the above theory have a significant effect and decrease the limit further to below the theoretical value given by Eq. (7.43).

While the aerodynamic characteristics of fixed-wing kites can modulated rapidly to low and even negative values of the lift-to-drag ratio (close to zero and negative angle of attack), this is not possible with soft-wing kites. The actuation of this type of kite is slower and, for reasons of structural stability, restricted to a positive lift-to-drag ratio (positive angle of attack). Because of this, we implement the reel-in phase with a constant, prescribed lift-to-drag ratio $E$ and a dependent elevation angle $\beta$. In this case, the nondimensional tether force and tractive power during the reel-in phase can be derived by inserting Eq. (7.40) into Eqs. (7.15) and (7.16)

$$\frac{F_\mathrm{t}}{qS} = C_\mathrm{L}\sqrt{1+\frac{1}{E^2}}\frac{\left(\sqrt{1+E^2\left(1-f^2\right)}-f\right)^2}{1+E^2}, \tag{7.44}$$

$$\frac{P}{P_\mathrm{w}S} = C_\mathrm{L}\sqrt{1+\frac{1}{E^2}}f\frac{\left(\sqrt{1+E^2\left(1-f^2\right)}-f\right)^2}{1+E^2}. \tag{7.45}$$

Compared to Eqs. (7.25) and (7.26), the above expressions miss the factor $1+E^2$, which especially for $E \gg 1$ is reflecting the substantial amplification of the tether force and tractive power in the reel-out phase flying crosswind maneuvers.

### Mechanical Cycle Power

Expressing the tether force during the reel-out phase by Eq. (7.25), and during the reel-in phase by Eq. (7.44), the net mechanical energy per cycle can be calculated with the known tether length change as

$$E_\mathrm{c} = E_\mathrm{o} + E_\mathrm{i} = \left[F_\mathrm{t,o} - F_\mathrm{t,i}\right](r_\mathrm{max} - r_\mathrm{min}), \tag{7.46}$$

$$= qS\left[\gamma_\mathrm{o}\left(\cos\beta_\mathrm{o} - f_\mathrm{o}\right)^2 - \gamma_\mathrm{i}\frac{\left(\sqrt{1+E^2\left(1-f^2\right)}-f\right)^2}{1+E^2}\right](r_\mathrm{max} - r_\mathrm{min}), \tag{7.47}$$

where the nondimensional aerodynamic force factors for the reel-out and reel-in phases are defined as

$$\gamma_\mathrm{o} = C_\mathrm{L,o}\sqrt{1+\frac{1}{E_\mathrm{o}^2}}\left(1+E_\mathrm{o}^2\right), \tag{7.48}$$

$$\gamma_\mathrm{i} = C_\mathrm{L,i}\sqrt{1+\frac{1}{E_\mathrm{i}^2}}. \tag{7.49}$$

The average mechanical power is determined by dividing the net energy per cycle by the time duration of a cycle. Neglecting the transition phases, the cycle time is determined as the sum of the reel-in time $t_\mathrm{i} = t_3 - t_0$ and reel-out time $t_\mathrm{o} = t_5 - t_3$

$$t_\mathrm{c} = t_\mathrm{i} + t_\mathrm{o} = \frac{r_\mathrm{min} - r_\mathrm{max}}{f_\mathrm{i} v_\mathrm{w}} + \frac{r_\mathrm{max} - r_\mathrm{min}}{f_\mathrm{o} v_\mathrm{w}}, \tag{7.50}$$

$$= \frac{r_\mathrm{max} - r_\mathrm{min}}{v_\mathrm{w}} \frac{f_\mathrm{i} - f_\mathrm{o}}{f_\mathrm{i} f_\mathrm{o}}, \tag{7.51}$$

where $t_0$, $t_3$, and $t_5$ are defined as illustrated in Fig. 7.11. Defining a normalized average mechanical power or, in short, normalized cycle power and substituting $E_\mathrm{c}$ by Eq. (7.47) and $t_\mathrm{c}$ by Eq. (7.51) lead to

$$p_\mathrm{c} = \frac{E_\mathrm{c}}{t_\mathrm{c} P_\mathrm{w} S \gamma_\mathrm{o}} = \left[ (\cos\beta_\mathrm{o} - f_\mathrm{o})^2 - \frac{\gamma_\mathrm{i}}{\gamma_\mathrm{o}} \frac{\left(\sqrt{1 + E^2\left(1 - f^2\right)} - f\right)^2}{1 + E^2} \right] \frac{f_\mathrm{i} f_\mathrm{o}}{f_\mathrm{i} - f_\mathrm{o}}, \tag{7.52}$$

with the aerodynamic force factors $\gamma_\mathrm{o}$ and $\gamma_\mathrm{i}$ defined in Eqs. (7.48) and (7.49), respectively. Since the generated energy generally is the dominating contribution to the cycle power, the force factor of the reel-out phase is used for the normalization, such that the ratio $\gamma_\mathrm{i}/\gamma_\mathrm{o}$ quantifies the relative effect of the consumed energy. From Eq. (7.52), the average cycle power can be evaluated as

$$P_\mathrm{c} = \frac{E_\mathrm{c}}{t_\mathrm{c}} = p_\mathrm{c} \gamma_\mathrm{o} P_\mathrm{w} S. \tag{7.53}$$

### 7.3.4 Performance Optimization Under Operational Constraints

Considering only the reel-out phase, the extreme value of the third-order polynomial in $f$ on the right-hand side of Eq. (7.26) leads to the optimal reeling factor and corresponding optimal tractive power expressions (Luchsinger 2013)

$$f_\mathrm{opt} = \frac{1}{3}\cos\beta_\mathrm{o}, \tag{7.54}$$

$$\zeta_\mathrm{opt} = \frac{4}{27}\cos^3\beta_\mathrm{o}\gamma_\mathrm{o}. \tag{7.55}$$

$$P_\mathrm{opt} = \frac{4}{27}\cos^3\beta_\mathrm{o}\gamma_\mathrm{o} P_\mathrm{w} S. \tag{7.56}$$

The expressions reflect the well-known dependencies of kite-based energy harvesting on key environmental, operational, and design parameters. The optimal reel-out speed

is one-third of the wind speed when the tether is parallel to the ground, from where it progressively decreases with increasing elevation angle. As typical for wind energy converters, the tractive power $P_{\mathrm{opt}}$ increases with the cube of the wind speed stemming from the wind power density $P_{\mathrm{w}}$ given by Eq. (7.18). It decreases with the cubed cosine of the elevation angle, stressing the importance of maintaining an as low as possible elevation angle during reel out. To maximize the aerodynamic force factor $\gamma_{\mathrm{o}}$, we note that for crosswind operation, the contribution of the tether to the total system drag sets a hard lower limit for the minimum system drag. For this reason, aerodynamic optimization is primarily about maximizing the lift coefficient of the kite.

Nevertheless, the theoretical performance projected by Eq. (7.56) is practically not achievable. On the one hand, the reel-in phase and other inherent conversion losses cannot be neglected. On the other hand, any real system is subject to hardware limits that need to be considered when optimizing the system's operation. Important performance envelope borders originate from the maximum tensile force the tether can withstand and the maximum electrical power the generator can produce. The derivations so far have not considered these hardware limitations.

In the following, the maximum normalized cycle power is determined for three operational regimes. In the first regime, the wind speeds are sufficiently low that hardware limitations do not need to be considered. Accordingly, the cycle power is determined by optimizing the reeling speeds in both phases of the idealized cycle. In the second regime, the wind speeds have increased to a level where the maximum allowed tether force is reached in the reel-out phase. To keep the tether force at this limit, the reel-out speed is now increased with the wind speed, and only the reeling speed can be optimized to maximize the cycle power. In the third regime, the wind speeds have increased further to a level where also the maximum allowed generator power is reached. To comply with the joint force and power limits, the reel-out speed cannot be increased any further. Instead, the aerodynamic properties of the kite or other operational parameters, such as the average elevation angle during reel-out, must be adjusted. As in the second regime, only the reel-in speed can be optimized to maximize the cycle power. The section is concluded by combining the three wind speed regimes within a single operation strategy.

### Wind Speed Regime 1: Unconstrained Operation

At sufficiently low wind speeds, neither the maximum tether tension nor the maximum generator power is reached. With given set values $\beta_{\mathrm{o}}$ and $E_{\mathrm{i}}$ for the elevation angle during reel-out and the lift-to-drag ratio during reel-in, the normalized cycle power given by Eq. (7.52) can be maximized by optimizing the reeling factors, $f_{\mathrm{o}}$ and $f_{\mathrm{i}}$,

$$p_{\mathrm{c,opt}} = \max_{f_\mathrm{o}, f_\mathrm{i}} \left\{ \left[ (\cos\beta_\mathrm{o} - f_\mathrm{o})^2 - \frac{\gamma_\mathrm{i}}{\gamma_\mathrm{o}} \frac{\left(\sqrt{1 + E_\mathrm{i}^2 \left(1 - f_\mathrm{i}^2\right)} - f_\mathrm{i}\right)^2}{1 + E_\mathrm{i}^2} \right] \frac{f_\mathrm{i} f_\mathrm{o}}{f_\mathrm{i} - f_\mathrm{o}} \right\}. \tag{7.57}$$

For unconstrained operation, the aerodynamic force factors $\gamma_\mathrm{i}$ and $\gamma_\mathrm{o}$ are assumed to be constant.

### Wind Speed Regime 2: Constrained Tether Force

The first hardware limit that is generally encountered during the reel-out phase is the maximum allowed tether force, also denoted as rated or nominal tether force. Using Eqs. (7.25, (7.17), and (7.48), the tether force during the reel-out phase can be formulated as

$$F_\mathrm{t,o} = \frac{1}{2} \rho v_\mathrm{w}^2 S \gamma_\mathrm{o} (\cos\beta_\mathrm{o} - f_\mathrm{o})^2 , \tag{7.58}$$

which, when reaching the nominal force, evaluates to

$$F_\mathrm{t,n} = \frac{1}{2} \rho v_\mathrm{n,F}^2 S \gamma_\mathrm{o} \left(\cos\beta_\mathrm{o} - f_\mathrm{n,F}\right)^2 , \tag{7.59}$$

where $v_\mathrm{n,F}$ and $f_\mathrm{n,F}$ are the wind speed and reeling factor at which this specific condition occurs. The nominal values $F_\mathrm{t,n}$, $v_\mathrm{n,F}$, and $f_\mathrm{n,F}$ are constant properties of a specific AWE system. An effective strategy to limit the tether force to the nominal value also for larger wind speeds is a controlled increase of the reeling speed. The reeling factor required to impose the constraint $F_\mathrm{t,o} = F_\mathrm{t,n}$ for $v_\mathrm{w} > v_\mathrm{n,F}$ can be derived by combining Eqs. (7.25) and (7.59) to

$$\frac{1}{2} \rho v_\mathrm{w}^2 S \gamma_\mathrm{o} (\cos\beta_\mathrm{o} - f_\mathrm{o})^2 = \frac{1}{2} \rho v_\mathrm{n,F}^2 S \gamma_\mathrm{o} \left(\cos\beta_\mathrm{o} - f_\mathrm{n,F}\right)^2 , \tag{7.60}$$

which, assuming a constant aerodynamic force factor $\gamma_\mathrm{o}$ and elevation angle $\beta_\mathrm{o}$, leads to

$$f_\mathrm{o} = \frac{\cos\beta_\mathrm{o} (\mu_\mathrm{F} - 1) + f_\mathrm{n,F}}{\mu_\mathrm{F}}. \tag{7.61}$$

In the above expression, we introduced the nondimensional velocity parameter

$$\mu_\mathrm{F} = \frac{v_\mathrm{w}}{v_\mathrm{n,F}} > 1, \tag{7.62}$$

which quantifies how much the wind speed exceeds the nominal value. Equation (7.61) describes how, starting from $f_{\mathrm{n,F}}$ at $v_{\mathrm{n,F}}$, the reeling factor $f_{\mathrm{o}}$ increases with increasing wind speed $v_{\mathrm{w}}$ in regime 2. Since the tether force during the reel-in phase is much lower than during the reel-out phase, the reeling factor $f_{\mathrm{i}}$ can be varied freely to maximize the cycle power. The mechanical power during the reel-out phase is given by

$$P_{\mathrm{o}} = F_{\mathrm{t,n}} v_{\mathrm{w}} f_{\mathrm{n,F}}. \tag{7.63}$$

Using Eq. (7.61) to substitute the reeling factor $f_{\mathrm{o}}$ in Eq. (7.51) leads to the following expression for the cycle time:

$$t_{\mathrm{c}} = \frac{r_{\max} - r_{\min}}{v_{\mathrm{w}}} \frac{\mu_{\mathrm{F}} f_{\mathrm{i}} - \left[(\mu_{\mathrm{F}} - 1)\cos\beta_{\mathrm{o}} + f_{\mathrm{n,F}}\right]}{f_{\mathrm{i}}\left[(\mu_{\mathrm{F}} - 1)\cos\beta_{\mathrm{o}} + f_{\mathrm{n,F}}\right]}. \tag{7.64}$$

The net mechanical energy per cycle can be defined similarly to Eqs. (7.46) and (7.47), but now replacing the reel-out tether force $F_{\mathrm{t,o}}$ first by the nominal tether force $F_{\mathrm{t,n}}$, which is then resolved by a combination of Eqs. (7.59) and (7.62),

$$\begin{aligned} E_{\mathrm{c}} &= \left[F_{\mathrm{t,n}} - F_{\mathrm{t,i}}\right](r_{\max} - r_{\min}), \\ &= qS\gamma_{\mathrm{o}} \left[\frac{1}{\mu_{\mathrm{F}}^2}\left(\cos\beta_{\mathrm{o}} - f_{\mathrm{n,F}}\right)^2 \right. \\ &\qquad \left. - \frac{\gamma_{\mathrm{i}}}{\gamma_{\mathrm{o}}} \frac{\left(\sqrt{1 + E_{\mathrm{i}}^2\left(1 - f_{\mathrm{i}}^2\right)} - f_{\mathrm{i}}\right)^2}{1 + E_{\mathrm{i}}^2}\right](r_{\max} - r_{\min}). \end{aligned} \tag{7.65}$$

The factor $1/\mu_{\mathrm{F}}^2$ is responsible for a rapid decrease of the generated energy contribution when the wind speeds exceed the nominal value. The normalized cycle power can be formulated in analogy to Eq. (7.52). Substituting $E_{\mathrm{c}}$ by Eq. (7.65) and $t_{\mathrm{c}}$ by Eq. (7.64) gives

$$\begin{aligned} p_{\mathrm{c}} = &\left[\frac{1}{\mu_{\mathrm{F}}^2}\left(\cos\beta_{\mathrm{o}} - f_{\mathrm{n,F}}\right)^2 \right. \\ &\left. - \frac{\gamma_{\mathrm{i}}}{\gamma_{\mathrm{o}}} \frac{\left(\sqrt{1 + E_{\mathrm{i}}^2\left(1 - f_{\mathrm{i}}^2\right)} - f_{\mathrm{i}}\right)^2}{1 + E_{\mathrm{i}}^2}\right] \frac{f_{\mathrm{i}}\left[(\mu_{\mathrm{F}} - 1)\cos\beta_{\mathrm{o}} + f_{\mathrm{n,F}}\right]}{\mu_{\mathrm{F}} f_{\mathrm{i}} - \left[(\mu_{\mathrm{F}} - 1)\cos\beta_{\mathrm{o}} + f_{\mathrm{n,F}}\right]}, \end{aligned} \tag{7.66}$$

which can be maximized by optimizing the reeling factor $f_\mathrm{i}$,

$$p_{\mathrm{c,opt}} = \max_{f_\mathrm{i}} \left\{ \left[ \frac{1}{\mu_\mathrm{F}^2} \left(\cos\beta_\mathrm{o} - f_{\mathrm{n,F}}\right)^2 - \frac{\gamma_\mathrm{i}}{\gamma_\mathrm{o}} \frac{\left(\sqrt{1+E_\mathrm{i}^2\left(1-f_\mathrm{i}^2\right)} - f_\mathrm{i}\right)^2}{1+E_\mathrm{i}^2} \right] \frac{f_\mathrm{i}\left[(\mu_\mathrm{F}-1)\cos\beta_\mathrm{o} + f_{\mathrm{n,F}}\right]}{\mu_\mathrm{F} f_\mathrm{i} - \left[(\mu_\mathrm{F}-1)\cos\beta_\mathrm{o} + f_{\mathrm{n,F}}\right]} \right\}. \tag{7.67}$$

Because the tether force limit is maintained by modulating the reeling speed only, the aerodynamic force factors $\gamma_\mathrm{i}$ and $\gamma_\mathrm{o}$ are assumed to be constant, as was the case for unconstrained operation.

### Wind Speed Regime 3: Constrained Tether Force and Generator Power

With the tether force being constrained to the nominal value, the second hardware limit encountered at increasing wind speeds is the maximum allowed generator power, also denoted as rated or nominal generator power. Because the mechanical power is the product of tether force and reeling speed, the reeling speed cannot be increased any further to compensate for higher wind speeds. Instead, the tether force is now limited by depowering the kite, adjusting its aerodynamic properties or other operational parameters. For example, Schelbergen et al. (2020) first increase the elevation angle during reel-out with increasing wind speeds, and only when this has reached a practical limit adjust also the aerodynamic properties. In the present work, we follow Luchsinger (2013) and adjust only the aerodynamic properties of the kite.

The nominal mechanical power of the generator can be evaluated as

$$P_\mathrm{n} = F_{\mathrm{t,n}} v_{\mathrm{n,P}} f_{\mathrm{n,P}}, \tag{7.68}$$

with the nominal tether force given by

$$F_{\mathrm{t,n}} = \frac{1}{2}\rho v_{\mathrm{n,P}}^2 S \gamma_\mathrm{o} \left(\cos\beta_\mathrm{o} - f_{\mathrm{n,P}}\right)^2, \tag{7.69}$$

where $v_{\mathrm{n,P}}$ and $f_{\mathrm{n,P}}$ represent the wind speed and reeling factor at which this specific nominal power value occurs. The parameters $P_\mathrm{n}$, $v_{\mathrm{n,P}}$, and $f_{\mathrm{n,P}}$ are properties of the specific system. The product $v_{\mathrm{n,P}} f_{\mathrm{n,P}}$ is the nominal reeling speed which is kept constant throughout this wind speed regime until reaching the cut-out wind speed at which the operation is terminated. Enforcing a constant reeling speed for $v_\mathrm{w} > v_{\mathrm{n,P}}$ is expressed as

$$v_\mathrm{w} f_\mathrm{o} = v_{\mathrm{n,P}} f_{\mathrm{n,P}}, \tag{7.70}$$

which leads to

$$f_{\mathrm{o}} = \frac{f_{\mathrm{n,P}}}{\mu_{\mathrm{P}}}, \tag{7.71}$$

where we introduced the nondimensional velocity factor

$$\mu_{\mathrm{P}} = \frac{v_{\mathrm{w}}}{v_{\mathrm{n,P}}} > 1. \tag{7.72}$$

Equation (7.71) describes how, starting from $f_{\mathrm{n,P}}$ at $v_{\mathrm{n,P}}$, the reeling factor $f_{\mathrm{o}}$ decreases with increasing wind speed $v_{\mathrm{w}}$ in regime 3. To also keep the tether force at the nominal value, the force factor $\gamma_{\mathrm{o}}$ needs to be reduced for $v_{\mathrm{w}} > v_{\mathrm{n,P}}$. From Eq. (7.58), we derive the following relation:

$$\gamma_{\mathrm{o}} = \frac{F_{\mathrm{t,n}}}{q\,S\,(\cos\beta_{\mathrm{o}} - f_{\mathrm{o}})^2}, \tag{7.73}$$

which replaces Eq. (7.48) in wind speed regime 3 to calculate the force factor during reel-out.

The differentiation of wind speed regimes 2 and 3 is based on the assumption that the nominal force $F_{\mathrm{t,n}}$ is reached at a lower wind speed than the nominal power $P_{\mathrm{n}}$, i.e., that $v_{\mathrm{n,P}} > v_{\mathrm{n,F}}$ (Luchsinger 2013; Schmehl et al. 2013). The values of nominal force and power depend on the specific design of the AWE system and are commonly a result of systematic trade-offs during the sizing of components.

Using Eq. (7.71) to substitute the reeling factor $f_{\mathrm{o}}$ in Eq. (7.51) leads to the following expression for the cycle time:

$$t_{\mathrm{c}} = \frac{r_{\max} - r_{\min}}{v_{\mathrm{w}}} \frac{\mu_{\mathrm{P}} f_{\mathrm{i}} - f_{\mathrm{n,P}}}{f_{\mathrm{i}} f_{\mathrm{n,P}}}. \tag{7.74}$$

The net mechanical energy per cycle can be defined similarly to Eqs. (7.46) and (7.47), but now replacing the reel-out tether force $F_{\mathrm{t,o}}$ by the nominal tether force $F_{\mathrm{t,n}}$, which is then resolved by a combination of Eqs. (7.69) and (7.72),

$$\begin{aligned} E_{\mathrm{c}} &= \left[F_{\mathrm{t,n}} - F_{\mathrm{t,i}}\right](r_{\max} - r_{\min}), \\ &= qS\gamma_{\mathrm{o}} \left[ \frac{1}{\mu_{\mathrm{P}}^2} \left(\cos\beta_{\mathrm{o}} - f_{\mathrm{n,P}}\right)^2 \right. \\ &\qquad \left. - \frac{\gamma_{\mathrm{i}}}{\gamma_{\mathrm{o}}} \frac{\left(\sqrt{1 + E_{\mathrm{i}}^2\left(1 - f_{\mathrm{i}}^2\right)} - f_{\mathrm{i}}\right)^2}{1 + E_{\mathrm{i}}^2} \right] (r_{\max} - r_{\min}). \end{aligned} \tag{7.75}$$

The factor $1/\mu_\mathrm{P}^2$ is responsible for a rapid decrease in the generated energy contribution when the wind speeds exceed the nominal value. The normalized cycle power can be formulated in analogy to Eq. (7.52). Substituting $E_\mathrm{c}$ by Eq. (7.75) and $t_\mathrm{c}$ by Eq. (7.74) gives

$$p_\mathrm{c} = \left[ \frac{1}{\mu_\mathrm{P}^2} \left(\cos\beta_\mathrm{o} - f_\mathrm{n,P}\right)^2 - \frac{\gamma_\mathrm{i}}{\gamma_\mathrm{o}} \frac{\left(\sqrt{1+E_\mathrm{i}^2\left(1-f_\mathrm{i}^2\right)} - f_\mathrm{i}\right)^2}{1+E_\mathrm{i}^2} \right] \frac{f_\mathrm{i} f_\mathrm{n,P}}{\mu_\mathrm{P} f_\mathrm{i} - f_\mathrm{n,P}}, \tag{7.76}$$

which can be maximized by optimizing the reeling factor $f_\mathrm{i}$,

$$p_\mathrm{c,opt} = \max_{f_\mathrm{i}} \left\{ \left[ \frac{1}{\mu_\mathrm{P}^2} \left(\cos\beta_\mathrm{o} - f_\mathrm{n,P}\right)^2 - \frac{\gamma_\mathrm{i}}{\gamma_\mathrm{o}} \frac{\left(\sqrt{1+E_\mathrm{i}^2\left(1-f_\mathrm{i}^2\right)} - f_\mathrm{i}\right)^2}{1+E_\mathrm{i}^2} \right] \frac{f_\mathrm{i} f_\mathrm{n,P}}{\mu_\mathrm{P} f_\mathrm{i} - f_\mathrm{n,P}} \right\}. \tag{7.77}$$

As mentioned above, the aerodynamic force factor $\gamma_\mathrm{o}$ is now modulated with the wind speed according to Eq. (7.73), while $\gamma_\mathrm{i}$ stays constant as given in Eq. (7.49).

### Three-Regime Strategy

To determine the maximum cycle power over the entire operational wind speed range, three different wind speed regimes are distinguished:

1. Low wind speeds, $v_\mathrm{w,min} \leq v_\mathrm{w} < v_\mathrm{n,F}$.
2. Medium wind speeds, $v_\mathrm{n,F} \leq v_\mathrm{w} < v_\mathrm{n,P}$.
3. High wind speeds, $v_\mathrm{n,P} \leq v_\mathrm{w} < v_\mathrm{w,max}$.

The threshold wind speeds $v_\mathrm{n,F}$ and $v_\mathrm{n,P}$ are determined by stepping through the entire wind speed range starting from the cut-in wind speed $v_\mathrm{w,min}$ and ending at the cut-out wind speed $v_\mathrm{w,max}$. In the low wind speed regime, Eq. (7.57) is maximized by optimizing the nondimensional reeling speeds $f_\mathrm{o}$ and $f_\mathrm{i}$. For each wind speed, the reel-out tether force $F_\mathrm{t,o}$ is computed from Eq. (7.58) and compared with the given nominal value $F_\mathrm{t,n}$ of the specific AWE system. Once $F_\mathrm{t,o}$ reaches $F_\mathrm{t,n}$, the system properties $v_\mathrm{n,F}$ and $f_\mathrm{n,F}$ are set to the current values of $v_\mathrm{w}$ and $f_\mathrm{o}$.

In the following medium wind speed regime, the reel-out tether force $F_\mathrm{t,o}$ is kept at the nominal allowable value $F_\mathrm{t,n}$ by increasing $f_\mathrm{o}$ with the wind speed according

to Eqs. (7.61) and (7.62). The maximum normalized cycle power given by Eq. (7.67) is determined by optimizing only $f_\mathrm{i}$. For each wind speed, the reel-out mechanical power $P_\mathrm{o}$ is computed from Eq. (7.63) and compared with the nominal value $P_\mathrm{n}$ of the specific AWE system. Once $P_\mathrm{o}$ reaches $P_\mathrm{n}$, the system properties $v_\mathrm{n,P}$ and $f_\mathrm{n,P}$ are set to the current values of $v_\mathrm{w}$ and $f_\mathrm{o}$.

In the following high wind speed regime, the tether force $F_\mathrm{t,o}$ and mechanical power $P_\mathrm{o}$ are kept at their nominal allowable values $F_\mathrm{t,n}$ and $P_\mathrm{n}$ by jointly decreasing $f_\mathrm{o}$ with increasing wind speed according to Eqs. (7.71) and (7.72) and $\gamma_\mathrm{o}$ according to Eq. (7.73). The maximum normalized cycle power given by Eq. (7.77) is determined by optimizing only $f_\mathrm{i}$.

The computed power curve of a representative AWE system for Mars conditions is illustrated in Fig. 7.14 and additional operational parameters in Fig. 7.15. The corresponding model input parameters are listed in Table 7.6. The performance of the system is evaluated in three different wind speed regimes, as outlined above, not accounting for component efficiencies or any other losses. In lack of aerodynamic characteristics of kites flying on Mars, the characteristics of kites from terrestrial AWE applications were adopted (Oehler and Schmehl 2019; Roullier 2020). All other machine-specific parameters and limits in Table 7.6 result from a preliminary sizing of system components (Rodriguez 2022).

The power curve exhibits the following behavior. Up to a wind speed of around 30 m/s, the reel-out power $P_\mathrm{o}$ closely tracks the optimal power $P_\mathrm{opt}$ defined by Eq. (7.56). Above this wind speed, $P_\mathrm{o}$ increases slower and, upon reaching the nominal wind speed, $v_\mathrm{n,P}$ levels out at the nominal value $P_\mathrm{n}$. The magnitude of the reel-in power $P_\mathrm{i}$ continuously increases with the wind speed, up to 41 m/s, when it suddenly drops again. The cycle power $P_\mathrm{c}$ reflects the combined effect of the two phase contributions, reaching its maximum $P_\mathrm{c,max} = 34.4$ kW at the nominal wind speed $v_\mathrm{n,P} = 34.8$ m/s.

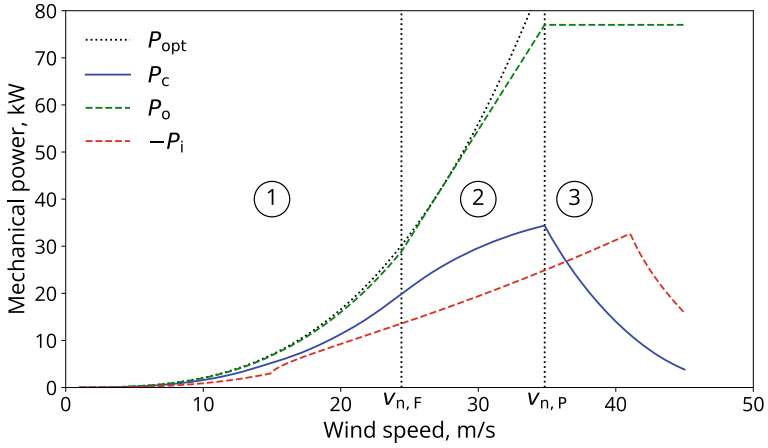


**Fig. 7.14** Power curve in three wind speed regions: ① unconstrained operation, ② constrained tether force, and ② constrained tether force and generator power

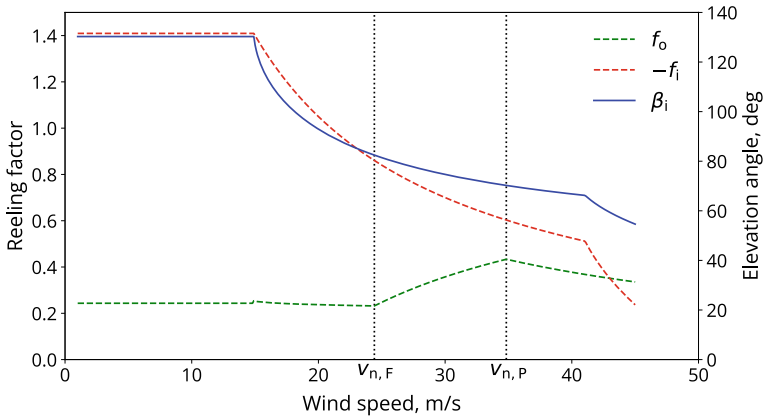


**Fig. 7.15** Operational parameters in three wind speed regions

**Table 7.6** Model input parameters

| Parameter | Value |
|---|---|
| Atmospheric density, $\rho$ (kg/m$^3$) | 0.01 |
| Elevation angle reel-out phase, $\beta_o$ (°) | 25 |
| Tether minimum reeling speed, $v_{k,r,min}$ (m/s) | −21 |
| Tether maximum reeling speed, $v_{k,r,max}$ (m/s) | 8 |
| Tether minimum deployed length, $r_{min}$ (m) | 240 |
| Tether maximum deployed length, $r_{max}$ (m) | 385 |
| Kite planform area, $S$ (m) | 200 |
| Kite lift coefficient reel-out phase, $C_{L,o}$ | 0.71 |
| Kite drag coefficient reel-out phase, $C_{D,k,o}$ | 0.14 |
| Kite lift coefficient reel-in phase, $C_{L,i}$ | 0.39 |
| Kite drag coefficient reel-in phase, $C_{D,k,i}$ | 0.39 |
| Tether drag coefficient, $C_{D,t}$ | 1.1 |
| Tether diameter, $d_t$ (mm) | 4.84 |
| Nominal tether force, $F_{t,n}$ (kN) | 5.1 |
| Nominal generator power, $P_n$, (kW) | 77 |

Above this wind speed, $P_c$ drops rapidly, which is largely an effect of the constant reel-out power while the reel-in power increases.

Figure 7.15 indicates that up to a wind speed of around 15 m/s, the reeling factors $f_o$ and $f_i$ are nearly constant. Above this value, the reel-in factor and the reel-in elevation angle $\beta_i$ drop abruptly in magnitude. The reel-out factor, on the other hand, stays roughly constant up to the nominal wind speed $v_{n,F} = 24.4$ m/s. Above this value, the reel-out factor increases to reach a maximum at $v_{n,P}$ and then decreases again. This behavior of $f_o$—constant in regime 1, increasing in regime 2, and again

decreasing in regime 3—illustrates the three-regime strategy discussed above. At a wind speed of 41 m/s, where the magnitude of the reel-in power sharply drops, also the magnitude of the reel-in factor and the reel-in elevation angles exhibit sharp drops. A sensitivity analysis indicates that several of the operational parameters and kite properties have a strong effect on the performance of the system. One example is the minimum reeling speed $v_{\mathrm{k,r,min}}$, which, when lowered, significantly increases the rated power $P_{\mathrm{c,max}}$.

The proposed performance model differs from Luchsinger (2013) in several aspects. Firstly, the elevation angle during the reel-out and reel-in phases is implemented consistently for all three wind speed regimes. A constant lift-to-drag ratio of the kite is prescribed for the reel-in phase, rendering the reel-in elevation angle dependent on the wind speed. In contrast to this, Luchsinger (2013) prescribed a constant reel-in elevation angle, rendering the lift-to-drag ratio dependent on the wind speed. While this is a reasonable approach for modeling fixed-wing kites, which can operate at negative and positive angles of attack, it is not feasible for soft-wing kites, which, for stability reasons, require a safe distance from negative angles of attack. The overall advantage of the proposed performance model and optimization procedure is the low computational cost.

### *7.3.5 Additional Power Conversion Losses*

So far, we have only considered the conversion of wind energy into mechanical net power. However, the conversion of mechanical into electrical net power via a cyclic process involving energy production, temporary storage, and consumption entails additional losses. These depend on the design and specification of the ground station and the operating conditions. We adopt the approach of Fechner and Schmehl (2013) to account for the conversion efficiencies of the alternating generator and motor modes. Other losses caused by the charging and discharging of the integrated battery/capacitor module, auxiliary drives, and the thermal control are neglected in the present ground station analysis, for the purpose of simplicity. Further details about the ground station analysis are available in Corte Vargas et al. (2022).

#### Generator Efficiency

According to Fechner and Schmehl (2013), assuming an identical, constant efficiency for generator and motor modes overestimates the overall conversion efficiency. Instead, they recommended modeling the component efficiencies as functions of the rotational speed of the drum and the applied torque.

The efficiency of the electrical machine in generator mode is defined as the ratio of electrical to mechanical power during the reel-out phase,

$$\eta_{\mathrm{e,o}} = \frac{P_{\mathrm{e,o}}}{P_{\mathrm{o}}}, \tag{7.78}$$

where

$$P_{\mathrm{o}} = F_{\mathrm{t,o}} v_{\mathrm{w}} f_{\mathrm{o}}. \tag{7.79}$$

The electrical power can also be evaluated by subtracting the conversion losses from the mechanical power,

$$P_{\mathrm{e,o}} = P_{\mathrm{o}} - L_{\mathrm{e,o}} - \tau_{\mathrm{f,o}} \omega_{\mathrm{o}}, \tag{7.80}$$

where $L_{\mathrm{e,o}}$ represents the electrical losses associated with current flow and generator resistance, and $\tau_{\mathrm{f,o}} \omega_{\mathrm{o}}$ the friction losses caused by the rotation of the drum with the angular velocity $\omega_{\mathrm{o}}$ against the friction torque $\tau_{\mathrm{f,o}}$. The reel-out speed of the tether and the angular velocity of the drum are coupled by the kinematic relation

$$v_{\mathrm{w}} f_{\mathrm{o}} = r_{\mathrm{d}} \omega_{\mathrm{o}}, \tag{7.81}$$

where $r_{\mathrm{d}}$ is the drum radius. The electrical losses are calculated from

$$L_{\mathrm{e,o}} = 3 R_{\mathrm{g}} I_{\mathrm{o}}^2 k, \tag{7.82}$$

where $I_{\mathrm{o}}$ denotes the electrical current, $R_{\mathrm{g}}$ the stage resistance, and $k$ a constant factor accounting for other not explicitly modeled machine losses. The formulation of Eq. (7.82) implies $k \geq 1$. The electrical current is computed as

$$I_{\mathrm{o}} = \tau_{\mathrm{g}} c_{\mathrm{g}}, \tag{7.83}$$

where $\tau_{\mathrm{g}}$ is the effective generator torque and $c_{\mathrm{g}}$ the generator constant. Assuming a quasi-steady rotation of the drum during the reel-out phase, the effective generator torque can be defined as

$$\tau_{\mathrm{g}} = F_{\mathrm{t,o}} r_{\mathrm{d}} - \tau_{\mathrm{f,o}}. \tag{7.84}$$

The friction torque $\tau_{\mathrm{f,o}}$ in Eqs. (7.80) and (7.84) can be modeled as an assembly of static and dynamic, velocity-dependent contributions

$$\tau_{\mathrm{f,o}} = \tau_{\mathrm{c}} + c_{\mathrm{v,f}} r_{\mathrm{d}} \omega_{\mathrm{o}}, \tag{7.85}$$

where $\tau_{\mathrm{c}}$ is the static friction torque, and $c_{v,f}$ the dynamic friction coefficient.

### Motor Efficiency

The efficiency of the electrical machine in motor mode is derived along the same lines, with the difference that electrical energy is now used to perform work against the aerodynamic forces acting on the kite. For this reason, the electrical efficiency in motor mode is defined as the ratio of mechanical to electrical power,

$$\eta_{\mathrm{e,i}} = \frac{P_{\mathrm{i}}}{P_{\mathrm{e,i}}}, \tag{7.86}$$

where

$$P_{\mathrm{i}} = F_{\mathrm{t,i}} v_{\mathrm{w}} f_{\mathrm{i}}. \tag{7.87}$$

Similar to Eq. (7.80), the electrical power can be evaluated by subtracting the conversion losses from the mechanical power,

$$P_{\mathrm{e,i}} = P_{\mathrm{i}} - L_{\mathrm{e,i}} - \tau_{\mathrm{f,i}} \omega_{\mathrm{i}}. \tag{7.88}$$

During reel-in, $P_{\mathrm{i}}$ and $P_{\mathrm{e,i}}$ are both negative, with $P_{\mathrm{e,i}} < P_{\mathrm{i}}$. Both loss contributions, $L_{\mathrm{e,i}}$ and $\tau_{\mathrm{f,i}} \omega_{\mathrm{i}}$ are positive. Similar to Eq. (7.81), the reel-in speed of the tether and the angular velocity of the drum are coupled by the kinematic relation

$$v_{\mathrm{w}} f_{\mathrm{i}} = r_{\mathrm{d}} \omega_{\mathrm{i}}. \tag{7.89}$$

Because $f_{\mathrm{i}}$ is negative, also $\omega_{\mathrm{i}}$ is negative, and, because $\tau_{\mathrm{f,i}} \omega_{\mathrm{i}}$ is positive, $\tau_{\mathrm{f,i}}$ is negative. Similar to Eq. (7.82), the electrical conversion losses are evaluated as a function of the passing current and phase resistance,

$$L_{\mathrm{e,i}} = 3 R_{\mathrm{m}} I_{\mathrm{i}}^2 k, \tag{7.90}$$

where the electrical current $I_{\mathrm{i}}$ is evaluated as the product of the motor constant $c_{\mathrm{m}}$ and the effective motor torque $\tau_{\mathrm{m}}$ required to drive the drum. As for the derivation of Eq. (7.84), we assume a quasi-steady rotation of the drum during the reel-in phase, defining the effective motor torque as

$$\tau_{\mathrm{m}} = F_{\mathrm{t,i}} r_{\mathrm{d}} - \tau_{\mathrm{f,i}}. \tag{7.91}$$

With $\tau_{\mathrm{m}}$ and $F_{\mathrm{t,i}} r_{\mathrm{d}}$ both positive and $\tau_{\mathrm{f,i}}$ negative, we can see that $\tau_{\mathrm{m}} > F_{\mathrm{t,i}} r_{\mathrm{d}}$ because the motor torque needs to overcome the additional friction torque $\tau_{\mathrm{f,i}}$ during reel-in.

### *7.3.6 Electrical Power Output*

The electrical net power production for a certain wind speed and atmospheric density is calculated by applying the efficiencies derived in Sect. 7.3.5 to the energy conversions during the reel-in and reel-out phases. To determine the energy produced over an entire Martian day, the probability at which the different wind speeds occur during this day needs to be factored in. This is the step in the analysis where the wind resource assessment is combined with the performance model.

### Electrical Cycle Power

Similar to the net mechanical energy per pumping cycle presented in Eq. (7.46), we can define the net electrical energy per cycle as

$$E_{\mathrm{e,c}} = E_{\mathrm{e,o}} + E_{\mathrm{e,i}}. \tag{7.92}$$

To determine the electrical cycle power, we introduce the conversion efficiencies defined in Eqs. (7.78) and (7.86),

$$P_{\mathrm{e,c}} = \frac{E_{\mathrm{e,o}} + E_{\mathrm{e,i}}}{t_o + t_i}, \tag{7.93}$$

$$= \frac{1}{t_{\mathrm{i}} + t_{\mathrm{o}}} \left( t_{\mathrm{o}} \eta_{\mathrm{e,o}} P_{\mathrm{o}} + t_{\mathrm{i}} \frac{1}{\eta_{\mathrm{e,i}}} P_{\mathrm{i}} \right). \tag{7.94}$$

It is important to note that, in the present study, the additional power conversion losses are taken into account only after determining the optimal mechanical cycle power $P_{\mathrm{c,opt}}$, as described in Sect. 7.3.4. This means the optimal point of operation maximizing the electrical cycle power can deviate from the purely mechanically determined optimum. In the frame of the presented feasibility analysis, we assume that this deviation is not significant. For a more refined analysis, this should however be taken into account.

### Daily Energy Production

As described in Sect. 7.2.4, the probability distribution of the wind speeds over a Martian day is described by a Weibull distribution function. For the performance analysis, we use a subdivision of the Martian year into 16 seasonal periods and the per-period constant Weibull parameters listed in Table 7.4. For the atmospheric density, we use the daily average function illustrated in Fig. 7.7, with linear interpolation in between the discrete data points.

Following the three-regime strategy presented in Sect. 7.3.4, the average electrical power per Martian day is evaluated by integrating the product of electrical cycle power and the corresponding wind speed probability over the three consecutive wind speed ranges

$$\begin{aligned} P_{\mathrm{e,d}} = &\int_{v_{\mathrm{w,min}}}^{v_{\mathrm{n,F}}} P_{\mathrm{e,c}}(v) g_{\mathrm{w}}(v)\, dv \\ &+ \int_{v_{\mathrm{n,F}}}^{v_{\mathrm{n,P}}} P_{\mathrm{e,c}}(v) g_{\mathrm{w}}(v)\, dv + \int_{v_{\mathrm{n,P}}}^{v_{\mathrm{w,max}}} P_{\mathrm{e,c}}(v) g_{\mathrm{w}}(v)\, dv. \end{aligned} \tag{7.95}$$

The lower bound of the first integral, $v_{w,min}$, is the cut-in wind speed at which the harvesting operation starts, while the upper bound of the last integral, $v_{w,max}$, is the cut-out wind speed at which the harvesting operation is discontinued.

With the average electrical power per Martian day, $P_{e,d}$, and the time duration of the day, $t_d$, the daily energy production of the AWE system is given by

$$E_{e,d} = t_d P_{e,d}. \tag{7.96}$$

### Annual Energy Production

The annual energy production (AEP) of the AWE system is determined by summing up the daily energy production over the 669 solar days of the Martian year

$$E_{e,y} = \sum_{d=1}^{669} E_{e,d}. \tag{7.97}$$

Because the wind power density defined by Eq. (7.18) depends on the atmospheric density, the power curve underlying Eq. (7.95) varies with the changing daily average density. The threshold wind speeds $v_{n,F}$ and $v_{n,P}$ vary with the density, as well as the shape of the power curve. For this reason, the power curve needs to be computed daily when evaluating Eq. (7.97). On the other hand, the Weibull parameters vary only with the 16 periods used for discretizing the seasonal effect on the wind speed statistics.

The energy production potential of different kite sizes is illustrated in Fig. 7.16. Table 7.7 summarizes the operational parameters used for the different kite sizes, while some other parameters were adapted from Table 7.6. Compared to the simu-

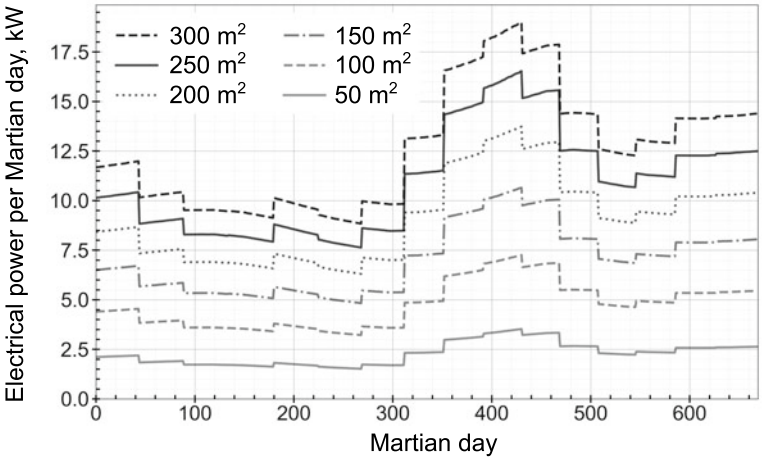


**Fig. 7.16** Average electrical power per Martian day for different kite sizes

**Table 7.7** Operational parameters for different kite sizes

| Kite planform area, $S$ ($m^2$) | 50 | 100 | 150 | 200 | 250 | 300 |
|---|---|---|---|---|---|---|
| Nominal tether force, $F_{t,n}$ (kN) | 1.7 | 3.1 | 4.1 | 5.1 | 6.3 | 7.2 |
| Nominal generator power, $P_n$ (kW) | 24 | 48 | 65 | 77 | 90 | 98 |
| Tether max. reeling speed, $v_{k,r,max}$ (m/s) | 8 | 8 | 8 | 8 | 8 | 8 |
| Tether min. reeling speed, $v_{k,r,min}$ (m/s) | −20 | −25 | −27 | −29 | −30 | −31 |
| Cut-in/out wind speed, $v_{w,min}$–$v_{w,max}$ (m/s) | 6–40 | 6–40 | 6–40 | 6–40 | 6–40 | 6–40 |

lation setup listed in Table 7.6, a more aggressive reel-in speed is used here for the system equipped with a 200 $m^2$ kite. The simulations show that the electric power scales roughly linearly with the planform area. This is expected because we use constant aerodynamic properties for the different kite sizes in this simplified analysis. The step changes of the Weibull parameters when advancing through the 16 seasonal periods are responsible for the discontinuities in the power output. The continuous variation of the power output within the seasonal periods results from the daily varying average density of the atmosphere.

## 7.4 Airborne Wind Energy in the Microgrid

As described in Sect. 7.2, the wind energy available at the habitat location exhibits substantial variations on daily and seasonal time scales. This is also reflected by the average daily power production of the AWE systems illustrated in Fig. 7.16. Much like a hybrid power plant on Earth (Reuchlin et al. 2023), a Martian microgrid must combine complementary renewable energy sources to ensure a reliable and uninterrupted power supply. With its ability to harness wind energy at higher altitudes, a kite power system can complement the power generated by solar panels, especially during periods of reduced solar irradiation, like, for example, during the night or during dust storms. On the other hand, solar panels can compensate for insufficient wind energy generation, adding robustness to the system design. Moreover, short-term electrical storage, such as rechargeable batteries, can store excess energy generated by the kite system and solar panels. This provides a backup power source during peak demand periods or when renewable energy generation is low (Ouroumova et al. 2021).

The simplified habitat energy model presented in this chapter is configured without long-term energy storage. While there still is a battery, it is relatively small and only used for buffering short-term fluctuations in power production, such as resulting from the pumping cycle operation. In Sect. 7.4.1, the power demand characteristics of the Martian habitat are examined. In Sect. 7.4.2, a daily supply and demand schedule is

formulated, based on the location-dependent resource characteristics. In Sect. 7.4.3, the framework model of the habitat energy system is first outlined and then used to compare the performance of different system configurations.

### 7.4.1 Habitat Power Demand

Because of varying daily activities, the electrical energy consumption of humans is generally irregular. Past research suggests that the mental and physical health of a habitat crew is best maintained by keeping a regular schedule for the entire mission because this helps synchronize the human circadian rhythm with the day-night cycle on Earth (Horneck et al. 2003; Basner et al. 2013). In the present study, we consider a timekeeping scheme based on Martian solar days (sols) of 24 Martian hours to aid human adaptation. Every hour consists of 60 Martian minutes, each comprising 60 Martian seconds. However, a second on Mars is approximately 1.0275 times longer than on Earth. We distinguish work and rest periods with different power consumption characteristics. While work periods require an average of 10 kW for scientific and domestic activities on top of the basic energy requirements of the habitat, rest periods require less power for maintaining basic habitat activities and covering the base loads of the life-support systems. Examining and interpreting data from experiments in the Hawaii Space Exploration Analog and Simulation (HI-SEAS) habitat (Barnard et al. 2019; Engler 2017; Engler et al. 2019), we propose a schedule alternating between 14 Martian work hours, lasting from 9:00 until 23:00, and 10 rest hours with energy requirements of 10 kW and 5 kW, respectively. For the present study, we use a constant daily energy demand[2] of 240 kWh (Ouroumova et al. 2021).

### 7.4.2 Power Generation and Demand Schedule

Once the power demand of the habitat is quantified, a schedule for the power generation from wind and solar resources can be established. Since the energy model is configured without long-term energy storage, seasonal variations of the renewable resources have to be taken into account, and the hybrid power plant must generate sufficient energy every day throughout the year. In the present study, we consider a fixed daily schedule accounting for the specific diurnal and seasonal variations of the wind and solar resources at the habitat location Arsia North described in Sect. 7.2.1.

[2] Energy units kWh and MWh refer to Martian hours.

### Wind Energy

The annual wind resource and its seasonal variation were evaluated in Sects. 7.2.3, 7.2.4, and 7.2.5. As illustrated in Fig. 7.5, the average wind speeds at the habitat location consistently drop below the considered minimum wind speeds between 9:00 and 11:00 and again between 19:00 and 21:00. Relying solely on wind power to meet the demand during these periods is thus unrealistic, which needs to be accounted for in the microgrid model. It is important to note that this characteristic of the wind resource is specific to the location on the planet. The wind resource varies substantially with latitude, as evidenced by the comparison of the wind speeds at Arsia North, a location near Mars' equator, with those at Deuteronilus Mensae, a very northern location (see Sect. 7.2.1) for which Ouroumova et al. (2021) found wind speeds dropping to very low values during the entire night.

To evaluate the wind power output for each day, the average production for the entire day is used. It is assumed that all the energy is generated within a 20-hour period of the day. Consequently, the average power levels estimated by the pumping kite model are scaled by a factor of 24/20.

### Solar Energy

The solar power output of the photovoltaic system is modeled as proportional to the solar irradiance at the habitat location. The hourly solar irradiance over the Martian year is available from the MCD and can be used to determine the power output of the solar PV system. From the extracted solar flux data visualized in Fig. 7.17, it is evident that power output consistently begins at about 6:00 throughout the Martian year and ends latest at 19:00. This behavior is once again correlated to

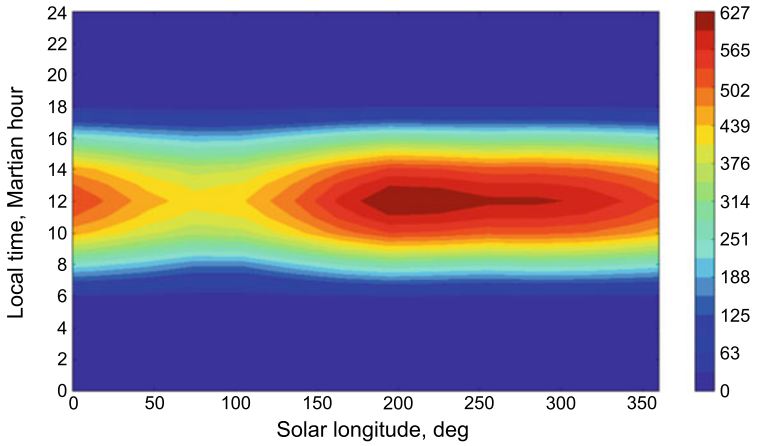


**Fig. 7.17** Solar flux over the Martian day along the Martian year at Arsia North

the specific location of the habitat close to the equator. For the previously studied northern location, Deuteronilus Mensae, the annual variation of sunrise and sunset times is substantial and needs to be taken into account in the modeling of the solar power output (Corte Vargas et al. 2022; Ouroumova et al. 2021).

### Combined Schedule

To develop the combined supply and demand schedule, the Martian day is divided into seven periods of different power requirements and energy source availabilities. These schedule periods are visualized in Fig. 7.18. Above the timeline is the generated power, comprising wind power $P_{\text{wind}}$ and solar power $P_{\text{solar}}$ contributions. Below the timeline is the habitat demand, comprising power demand $P_{\text{rest}}$ during resting time and power demand $P_{\text{work}}$ during working time. The third period was subdivided into two sub-periods, T31 and T32, to increase the accuracy of representing the solar resource. The periods have the following characteristics:

T0: 23:00 – 05:59 (7 h) Wind power output + rest level power demand.
T1: 06:00 – 08:59 (3 h) Wind + solar power output + rest level power demand.
T2: 09:00 – 10:59 (2 h) Solar power output + work level power demand.
T31: 11:00 – 14:59 (4 h) Wind + solar power output + work level power demand.
T32: 15:00 – 18:59 (4 h) Wind + solar power output + work level power demand.
T4: 19:00 – 20:59 (2 h) No power output + work level power demand.
T5: 21:00 – 22:59 (2 h) Wind power output + work level power demand.

For the numerical simulation, the average irradiance per hour is computed for the 24 months (periods of 28 or 27 Martian days) of the Martian year. Using this information, the average solar flux for the relevant four schedule periods, T1, T2, T31, and T32, is evaluated and presented in Fig. 7.19.

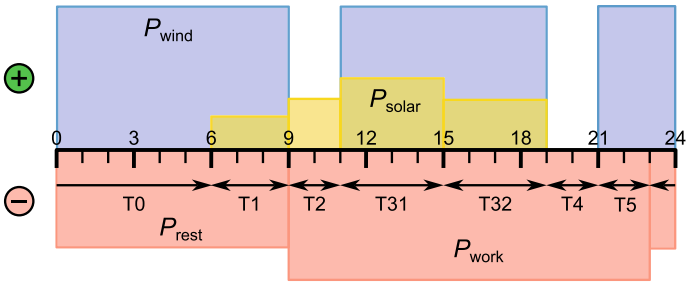


**Fig. 7.18** Sol power generation and demand schedule of habitat at Arsia North

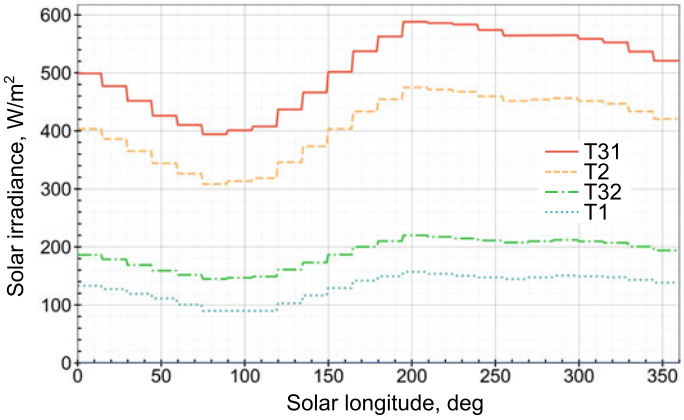


**Fig. 7.19** Average solar flux for the schedule periods with solar power production

### *7.4.3 Comparison of Different System Configurations*

The final step in the analysis is a comparison of different configurations of the habitat energy system. Transmission losses between the different components of the microgrid are taken into account in the energy system model. The modeling steps involve computing the wind and solar conditions for each day and for each schedule period within the day to meet the given daily power demand. The solar panel area is computed using the energy system model and adjusted by the maximum solar supply condition $k$. This set value determines the maximum irradiance for any day or schedule period. The remaining solar conditions are then computed based on the maximum irradiance. Auxiliary and dominant conditions are evaluated for each schedule period and day based on whether the wind or the solar condition is greater. The supply path is determined based on these conditions, assuming that the battery can meet the demand regardless of its actual charge. Finally, the supply deficit and surplus are evaluated for a set habitat demand, number of kites with planform area $S$, and the maximum solar condition $k$. This analysis helps identifying the days in the Martian year where the supply is insufficient and where there is a surplus, indicated by red and green colors, respectively. More details about the setup of the comparative analysis can be found in Rodriguez (2022).

Figure 7.20 illustrates the energy supply per day to the habitat for an energy system configuration with a single large kite. Setting the maximum solar supply condition of $k = 0.6$ means that per day and schedule period, the secondary energy supply is able to meet 60% of the habitat demand. The diagram indicates that the hybrid power plant can continuously provide a 10 kW power supply for most of the Martian year. The energy deficit can be seen as the red-shaded area.

Using two smaller kites instead of a single larger kite allows phase-shifted operation of the pumping kite power systems, which substantially reduces the required

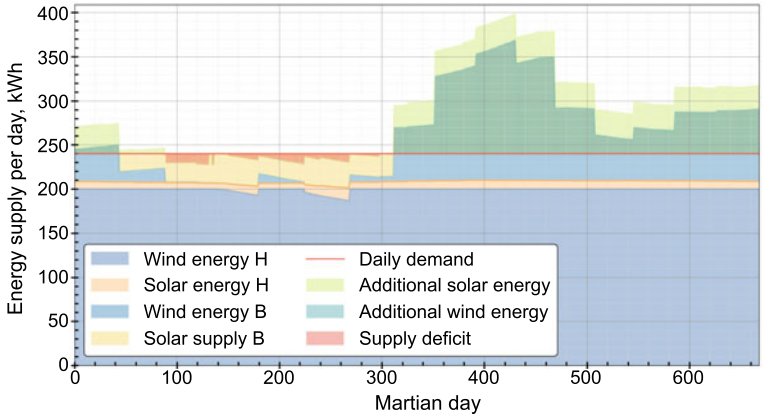


**Fig. 7.20** Computed energy supply per day, for a single kite with $S = 300\ \mathrm{m}^2$, $k = 0.6$. Abbreviations H and B in legend refer to habitat and battery, respectively

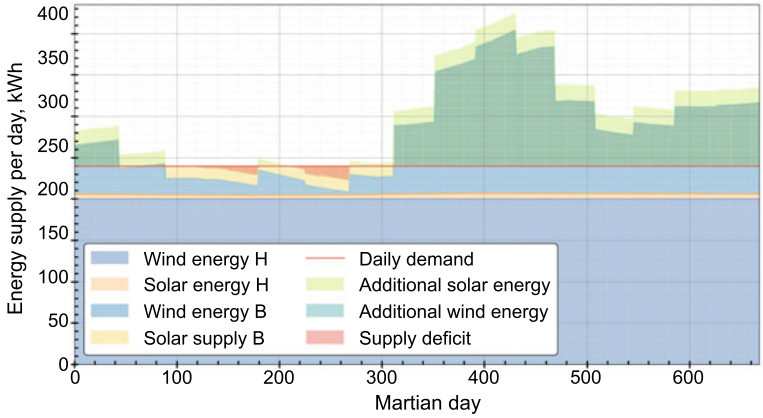


**Fig. 7.21** Computed energy supply per day, for two kites with $S = 150\ \mathrm{m}^2$, $k = 0.4$

battery storage capacity in the energy system. Figures 7.21, 7.22, and 7.23 illustrate the beneficial effect of using two smaller kites for increasing maximum solar supply conditions of $k = 0.4$, 0.5, and 0.6, respectively. The diagrams show that the better internal energetic balancing of two kite power systems in phase-shifted operation and the increasing solar component systematically decrease the energy deficit.

The presented computational framework allows for a comprehensive optimization of the habitat energy system configuration, balancing the primary and secondary sources of renewable energy, the integrated battery for short-term storage, and the habitat demand. It should be noted, however, that the illustrated configurations of the microgrid have only been selected for demonstration purposes.

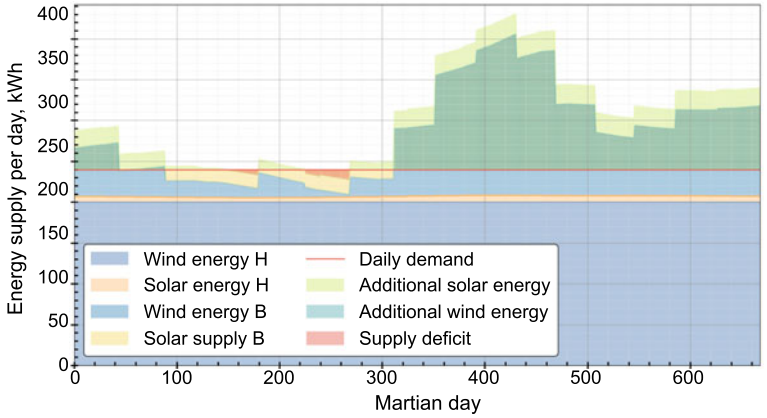


**Fig. 7.22** Computed energy supply per day, for two kites with $S = 150\ \mathrm{m}^2$, $k = 0.5$

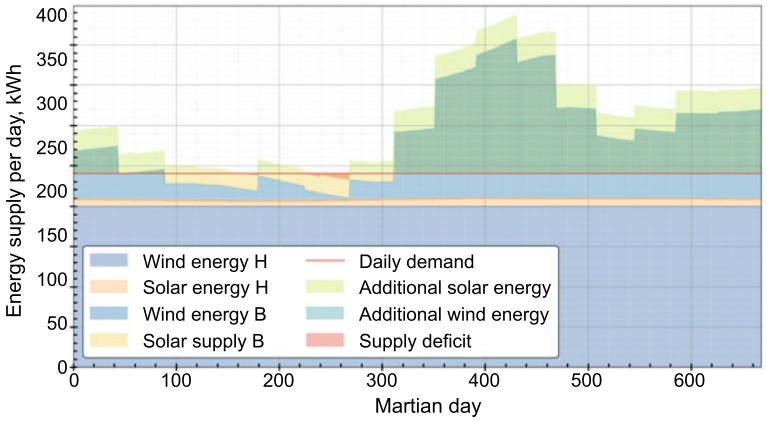


**Fig. 7.23** Computed energy supply per day, for two kites with $S = 150\ \mathrm{m}^2$, $k = 0.6$

## 7.5 Conclusions

In this chapter, we have demonstrated the technical feasibility of powering a habitat on Mars with renewable energies only, despite the challenging resource conditions. As the availability of resources for the construction of the habitat and its operation depends strongly on the location, the siting is of crucial importance. The site selected in this study, Arsia North, is a compromise between having suitable lava tubes available for constructing the subsurface habitat, and reasonable wind and solar energy resources.

To design the habitat's renewable energy system and analyze its performance, we have developed a comprehensive model of the hybrid power system, based on airborne wind energy (AWE), solar energy, and short-term battery storage. One key contribution of this work is the statistical description of the wind resource at the habitat location, using data extracted from the Mars Climate Database (MCD). The model provides the parameters of the Weibull distribution of the average wind speeds per day, at different operating heights for 16 different seasonal periods of the Martian year. Because the atmospheric density on Mars exhibits substantial diurnal and seasonal variations, a piecewise linear correlation is used to reproduce the day-to-day variations of the density along the year. To further improve the description of the wind resource in the future work, we suggest considering to use a weather research and forecasting model (WRF) to increase the spatial resolution of the MCD. We further suggest considering to use principal component analysis (PCA) and $k$-means clustering to develop characteristic vertical profiles and their probabilities from the available hourly wind speed data.

A second key contribution of this work is a performance model for the pumping cycle operation of a soft-kite-based AWE system. The model uses two representative quasi-steady flight states to discretize the pumping cycle, implementing a constant average elevation angle for the reel-out phase and a variable elevation angle for the reel-in phase. The model is used for systematic optimization of the operational parameters, to maximize the energy output for specific wind resource conditions and system specifications. To further improve the model in future work, we suggest accounting for the effect of gravity on the kite, which is particularly important during the reel-in phase. An additional measure to further increase the fidelity of the model is a numerical integration of the reel-in trajectory of the kite. This is particularly important for soft-kite systems with limited options to control the lift-to-drag ratio of the wing.

A final, third contribution of the work is the integration of the statistical resource description and performance model into a supply and demand framework model of the habitat's energy system. This framework model is used for balancing the electrical power from renewable energy resources, the short-term battery storage, and the habitat demand. It is also used for the sizing of the different system components and for investigating the effect of different configurations of the energy system. For the most part, the presented work was part of the project Rhizome and is summarized in Bier (2022).

**Data availability** The data and Python code used for this study are available from https://github.com/awegroup/awe_on_mars.

**Acknowledgements** R. S. has received financial support from the project Rhizome, funded by the European Space Agency (ESA).

## References


Anhalzer M, Abundio A, Zambrano J, Gurbanli Y, Zha G (2023) Transportation and energy ecosystem based on Martian atmosphere. In: AIAA SCITECH 2023 forum, 23–27 Jan 2023. National Harbor, MD & Online. https://doi.org/10.2514/6.2023-2474

Barnard A, Engler ST, Binsted K (2019) Mars habitat power consumption constraints, prioritization, and optimization. J Space Saf Eng 6(4):256–264. https://doi.org/10.1016/j.jsse.2019.10.006

Basner M, Dinges DF, Mollicone D, Ecker A, Jones CW, Hyder EC, Di Antonio A, Savelev I, Kan K, Goel N, Morukov BV, Sutton JP (2013) Mars 520-d mission simulation reveals protracted crew hypokinesis and alterations of sleep duration and timing. Proc Natl Acad Sci 110(7):2635–2640. https://doi.org/10.1073/pnas.1212646110

Bechtle P, Schelbergen M, Schmehl R, Zillmann U, Watson S (2019) Airborne wind energy resource analysis. Renew Energy 141:1103–1116. https://doi.org/10.1016/j.renene.2019.03.118

Bier H (2022) Rhizome: development of an autarkic design-to-robotic-production and operation system for building off-earth habitats (final report and movie). Dataset Rev 1 4TU ResearchData. https://doi.org/10.4121/19867561

Bier H, Hidding A, Latour M, Veere F, Peternel L, Schmehl R, Ourouvoma L, Cervone A, Verma M (2022) Rhizome: off-earth manufacturing and construction (of subsurface mars habitats). http://cs.roboticbuilding.eu/index.php/2019MSc3. Accessed 3 Aug 2022

Bluck J (2001) Antarctic/Alaska-like wind turbines could be used on Mars. https://www.nasa.gov/centers/ames/news/releases/2001/01_72AR.html. Accessed 3 Aug 2022

Boumis R (2017) The Average Wind Speed on Mars. https://sciencing.com/mars-earth-common-10034859.html . Accessed 3 Aug 2022

Corte Vargas F, Géczi M, Heidweiller S, Kempers MX, Klootwijk BJ, Marion F, Mordasov D van, Ouroumova LH, Terwindt EN, Witte D (2020) Arcadian renewable energy system: renewable energy for Mars habitat. B.Sc. Thesis, Delft University of Technology. http://resolver.tudelft.nl/uuid:93c343e5-ee79-4320-98a3-949d3e9c407d. Accessed 3 Aug 2022

Delgado-Bonal A, Martín-Torres FJ, Vázquez-Martín S, Zorzano MP (2016) Solar and wind exergy potentials for Mars. Energy 102:550–558. https://doi.org/10.1016/j.energy.2016.02.110

Diehl M (2013) Airborne wind energy: basic concepts and physical foundations. In: Ahrens U, Diehl M, Schmehl R (eds) Airborne wind energy. Green En- ergy and Technology (Chap 1). Springer, Berlin Heidelberg, pp 3–22. https://doi.org/10.1007/978-3-642-39965-7_1

Engler S (2017) Forecasting of Energy requirements for planetary exploration habitats using a modulated neural activation method. M.Sc. Thesis, University of Calgary. https://doi.org/10.11575/PRISM/26208.

Engler S, Binsted K, Leung H (2019) HI-SEAS habitat energy requirements and forecasting. Acta Astronaut 162:50–55. https://doi.org/10.1016/j.actaastro.2019.05.049

Fagiano L, Quack M, Bauer F, Carnel L, Oland E (2022) Autonomous air-borne wind energy systems: accomplishments and challenges. Ann Rev Control Robot Auton Syst 5(1):603–631. https://doi.org/10.1146/annurev-control-042820-124658

Fechner U, Schmehl R (2013) Model-based efficiency analysis of wind power conversion by a pumping kite power system. In: Ahrens U, Diehl M, Schmehl R (eds) Airborne wind energy. Green Energy and Technology (Chap 14). Springer, Berlin Heidelberg, pp 249–269. https://doi.org/10.1007/978-3-642-39965-7_10

Fechner U (232016) A methodology for the design of kite-power control systems. Ph.D. Thesis, Delft University of Technology. https://doi.org/10.4233/uuid:85efaf4c-9dce-4111-bc91-7171b9da4b77

Fechner U, Schmehl R (2018) Flight path planning in a turbulent wind environment. In: Schmehl R (ed) Airborne wind energy—advances in technology development and research. Green Energy and Technology (Chap 15). Springer, Singapore, pp 361–390. https://doi.org/10.1007/978-981-10-1947-0_15

Forget F, Hourdin F, Fournier R, Hourdin C, Talagrand O, Collins M, Lewis SR, Read PL, Huot JP (1999) Improved general circulation models of the Martian atmosphere from the surface to above 80 km. J Geophys Res Planets 104(E10):24155–24175. https://doi.org/10.1029/1999JE001025

Gallegos ZE, Newsom HE, Scuderi LA, Edge E (2019) Protonilus menasae: continued analysis of an exploration zone on the northern planetary di-chotomy of Mars. Prospects for future robotic and human missions. In: 50th Lunar and and planetary planetary science science conference, 18–22 Mar 2019. The Woodlands, Texas. https://www.hou.usra.edu/meetings/lpsc2019/pdf/3249.pdf

Gül D, Popescu Cabo A, Caruso M, Lange M de, Isidorova V, Kriharen Tiagoo K, Sanders L, Meyer Ranneft T, Klugt W van der, Sambath B (2021) AWESOM: airborne wind energy system on Mars. B.Sc. Thesis, Delft University of Technology. http://resolver.tudelft.nl/uuid:0298b063-7632-43f4-afa5-4065376df713. Accessed 3 Aug 2022

van Hagen L, Petrick K, Wilhelm S, Schmehl R (2023) Life-cycle assessment of a multi-megawatt airborne wind energy system. Energies 16(4):1750. https://doi.org/10.3390/en16041750

Hartwick VL, Toon OB, Lundquist JK, Pierpaoli OA, Kahre MA (2022) Assessment of wind energy resource potential for future human missions to Mars. Nat Astron 7:298–308. https://doi.org/10.1038/s41550-022-01851-4

Haslach H (1989) Wind Energy: a resource for a human mission to Mars. J Br Interplanet Soc 42:171–178

Head J, Dickson J, Mustard J, Milliken R, Scott D, Johnson B, Marchant D, Levy J, Kinch K, Hvidberg C, Forget F, Boucher D, Mikucki J, Fastook J, Klaus K (2015) Mars human science exploration and resource utilization: the di-chotomy boundary deuteronilus mensae exploration zone. In: First landing site/exploration zone workshop for human missions to the surface of Mars, 27–30 Oct 2015. Houston, Texas. https://www.nasa.gov/sites/default/files/atoms/files/exploration_zones_briefing_naochis_terra_deuteronilus_mensae_and_phlegra_dorsa_tagged.pdf. Accessed 18 Sept 2023

Holstein-Rathlou C, Thomas PE, Merrison J, Iversen JJ (2018) Wind turbine power production under current martian atmospheric conditions. In: Mars workshop on amazonian and present-day climate, Lakewood, Colorado, 18–22 June 2018. https://www.hou.usra.edu/meetings/amazonian2018/pdf/4004.pdf. Accessed 3 Aug 2022

Horneck G, Facius R, Reichert M, Rettberg P, Seboldt W, Manzey D, Comet B, Maillet A, Preiss H, Schauer L, Dussap CG, Poughon L, Belyavin A, Reitz G, Baumstark-Khan C, Gerzer R (2006) HUMEX, a study on the survivability and adaptation of humans to long-duration exploratory missions, part II: mis- sions to Mars. Adv Space Res 38(4):752–759. https://doi.org/10.1016/j.asr.2005.06.072

Horneck G, Facius R, Reichert M, Rettberg P, Seboldt W, Manzey D, Comet B, Maillet A, Preiss H, Schauer L, Dussap CG, Poughon L, Belyavin A, Reitz G, Baumstark-Khan C, Gerzer R (2003) Humex, a study on the survivability and adaptation of humans to long-duration exploratory missions, part I: lunar missions. Adv Space Res 31(11):2389–2401. https://doi.org/10.1016/S0273-1177(03)00568-4

James G, Chamitoff G, Barker D (1989) Resource utilization and site selection for a self-sufficient martian outpost. Technical Memorandum NASA/TM-98-206538. https://ntrs.nasa.gov/citations/19980147990. Accessed 3 Aug 2022

Joshi MM, Haberle R, Barnes J, Murphy J, Schaeffer J (1997) Low-level jets in the NASA Ames Mars general circulation model. J Geophys Res E Planets 102. https://doi.org/10.1029/96JE03765

Joshi MM, Lewis SR, Read PL, Catling DC (1995) Western boundary currents in the Martian atmosphere: numerical simulations and observational evidence. J Geophys Res 100(E3):5485–5500. https://doi.org/10.1029/94JE02716

KiteX (2023) Wind Catcher. http://kitex.tech/ Accessed 8 Jul 2023

Laboratoire de Météorologie Dynamique (2022) Martian climate database documentation. https://www-mars.lmd.jussieu.fr/mars/info_web/index.html. Accessed 5 Nov 2023

Luchsinger RH (2013) Pumping cycle kite power. In: Ahrens U, Diehl M, Schmehl R (eds) Airborne wind energy. Green Energy and Technology (Chap 3). Springer, Berlin Heidelberg, pp 47–64. https://doi.org/10.1007/978-3-642-39965-7_3

Millour E, Forget F, Spiga A, Vals M, Zakharov V, Montabone L, Lefevre F, Montmessin F, Chaufray JY, Lopez-Valverde M, Gonzalez-Galindo F, Lewis S, Read P, Desjean MC, Cipriani F, MCD/GCM Development Team (2018) The Mars climate database (Version 5.3). In: From Mars Express to ExoMars Scientific Workshop, ESA-ESAC, Madrid, Spain, 27–28 Feb 2018. https://ui.adsabs.harvard.edu/link_gateway/2018fmee.confE..68M/PUB_PDF. Accessed 3 Aug 2022

NASA (2023) NASA Mars helicopter. https://mars.nasa.gov/technology/helicopter. Accessed 15 Jun 2023

Nelson V (2020) Innovative wind turbines–an illustrated guidebook. CRC Press, Boca Raton, Florida. https://doi.org/10.1201/9781003010883

Oehler J, Schmehl R (2019) Aerodynamic characterization of a soft kite by in situ flow measurement. Wind Energy Sci 4(1):1–21. https://doi.org/10.5194/wes-4-1-2019

Ouroumova L, Witte D, Klootwijk B, Terwindt E, Marion F van, Mordasov D, Vargas FC, Heidweiller S, Géczi M, Kempers M, Schmehl R (2021) Combined airborne wind and photovoltaic energy system for Martian habitats. Spool 8(2):71–85. https://doi.org/spool.2021.2.6058

Qiu X, Ding C (2023) Radar observation of the lava tubes on the Moon and Mars. Remote Sens 15(11):2850. https://doi.org/10.3390/rs15112850

Reuchlin S, Joshi R, Schmehl R (2023) Sizing of hybrid power systems for off-grid applications using airborne wind energy. Energies 16(10). https://doi.org/10.3390/en16104036

Rodriguez M (2022) Airborne wind energy systems for Mars habitats. M.Sc. Thesis, Delft University of Technology. http://resolver.tudelft.nl/uuid:52a156ae-c758-4d3a-a403-54ce5fce2e5e. Accessed 15 Jun 2023

Roullier A (2020) Experimental analysis of a kite system's dynamics. M.Sc. Thesis, École Polytechnique Fédérale de Lausanne. https://doi.org/10.5281/zenodo.7752407

Salma V, Friedl F, Schmehl R (2019) Improving reliability and safety of airborne wind energy systems. Wind Energy 23(2):340–356. https://doi.org/10.1002/we.2433

Sauro F, Pozzobon R, Massironi M, De Berardinis P, Santagata T, De Waele J (2020) Lava tubes on Earth, Moon and Mars: a review on their size and morphology revealed by comparative planetology. Earth Sci Rev 209:103288. https://doi.org/10.1016/j.earscirev.2020.103288

Schelbergen M, Kalverla PC, Schmehl R, Watson SJ (2020) Clustering wind profile shapes to estimate airborne wind energy production. Wind Energy Sci 5(3):1097–1120. https://doi.org/10.5194/wes-5-1097-2020

Schmehl R (2019) Airborne wind energy—an introduction to an emerging technology. http://www.awesco.eu/awe-explained/. Accessed 3 Aug 2022

Schmehl R (2022) Power-generating kite flying on Mars? https://youtu.be/YS20vHhqgKk. Accessed 15 Jun 2023

Schmehl R, Noom M, Vlugt R van der (2013) Traction power generation with tethered wings. In: Ahrens U, Diehl M, Schmehl R (eds) Airborne wind energy. Green energy and technology (Chap 2). Springer, Berlin Heidelberg, pp 23–45. https://doi.org/10.1007/978-3-642-39965-7_2

Schorbach V, Weiland T (2022) Wind as a back-up energy source for Mars missions. Acta Astronaut 191:472–478. https://doi.org/10.1016/j.actaastro.2021.11.013

Silberg B (2012) Electricity in the air. https://climate.nasa.gov/news/727/electricity-in-the-air. Accessed 3 Aug 2022

Terink EJ (2009) Kiteplane flight dynamics. M.Sc. Thesis, Delft University of Technology. http://resolver.tudelft.nl/uuid:3e777823-ef53-4ac7-b246-cd7ff7b39487. Accessed 15 Jun 2023

Van der Vlugt R, Bley A, Schmehl R, Noom M (2019) Quasi-steady model of a pumping kite power system. Renew Energy 131:83–99. https://doi.org/10.1016/j.renene.2018.07.023

Van der Vlugt R, Peschel J, Schmehl R (2013) Design and experimental characterization of a pumping kite power system. In: Ahrens U, Diehl M, Schmehl R (eds) Airborne wind energy. Green Energy and Technology (Chap 23). Springer, Berlin Heidelberg, pp 403–425. https://doi.org/10.1007/978-3-642-39965-7_23

Vander Lind D (2013) Analysis and flight test validation of high performance airborne wind turbines. In: Ahrens U, Diehl M, Schmehl R (eds) Air-borne wind energy. Green Energy and Technology

(Chap 28). Springer, Berlin Heidelberg, pp 473–490. https://doi.org/10.1007/978-3-642-39965-7_28

Vermillion C, Cobb M, Fagiano L, Leuthold R, Diehl M, Smith RS, Wood TA, Rapp S, Schmehl R, Olinger D, Demetriou M (2021) Electricity in the air: insights from two decades of advanced control research and experimental flight testing of airborne wind energy systems. Ann Rev Control. https://doi.org/10.1016/j.arcontrol.2021.03.002

Williams DR (2020) Mars fact sheet. https://nssdc.gsfc.nasa.gov/planetary/factsheet/marsfact.html. Accessed 3 Aug 2022